MŰEGYETEM 1782

MSc. THESIS

A Fourier principle based Photoluminescence and visible Raman spectrometer

Sami Dzsaber

Thesis advisor: Ferenc Simon
Professor
Department of Physics
Institute of Physics
BME

Budapest University of Technology and Economics

BME
2015.

Contents

A szakdolgozat kiírása

A modern szilárdtestkutatás elengedhetetlen eszközei a spektrométerek. A spektroszkópiai módszerek egyik kiterjedtebb területe az optikai spektroszkópia. Laborunkban három éve fejlesztünk optikai spektrométereket, eddigi eredményeink: Fourier Transzform (FT) Raman spektrométer paramétereinek javítása, előkészületek látható lézeres FT-Raman spektroszkópiára, nagyérzékenységű fotolumineszcens (PL) spektrométer és optikailag detektált mágneses rezonancia (ODMR) spektrométer kifejlesztése. A jelentkező ebbe a kutatómunkába csatlakozna bele, a saját érdeklődésének is megfelelően választva az alábbi kutatási-fejlesztési területekből (akár többet is): - látható lézeres FT-Raman spektrométer paramétereinek javítása - FT-PL és FT-ODMR spektrométer kifejlesztése - az ODMR technika kiterjesztése nagy mágneses terű és kriogén környezetben való működés felé. - ezen spektrométerekkel végzett mérések szén alapú nanoszerkezeteken az elektronikus és rezgési tulajdonságaik vizsgálatára

Önállósági nyilatkozat

Alulírott Dzsaber Sami, a Budapesti Mûszaki és Gazdaságtudományi Egyetem hallgatója kijelentem, hogy ezt a szakdolgozatot meg nem engedett segédeszközök nélkül, saját magam készítettem, és csak a megadott forrásokat használtam fel. Minden olyan szövegrészt, adatot, diagramot, ábrát, amelyet azonos értelemben más forrásból átvettem, egyértelműen, a forrás megadásával megjelöltem.

Budapest, 2013. május 29.

Dzsaber Sami

Köszönetnyilvánítás

Köszönettel tartozom témavezetőmnek Prof. Simon Ferencnek, hogy bevezetett a kísérleti fizika világába. Hálával tartozom neki hogy, szakmai fejlődésemet éveken át gondozta. Köszönettel tartozom Negyedi Milánnak az optikában nyújtott segítségéért és Palotás Juliannának a minták elkészítéséért. Továbbá köszönettel tartozom Bernáth Bencének, Márkus Bencének és Gyüre Balázsnak, hogy segítettek elsajátítani a mikrohullámú technika alapjait. Hálával tartozom Prof. Thomas Pichlernek a Bécsi Egyetemről és Dr. Murányi Ferencnek az IT'IS alapítványtól, hogy részese lehettem kutató csoportjuknak szakmai gyakorlat keretében. Köszönettel tartozom a Fizika Tanszék munkatársainak, Bacsa Sándornak és Horváth Bélának a munkámhoz szükséges alkatrész munkák elkészítéséért. Hálával tartozom Dr. Fülöp Ferencnek az elektronikában nyújtott segítségéért. Továbbá hálával tartozom szüleimnek töretlen támogatásukért és, hogy megtanítottak a munka szeretetére. Végezetül hálával tartozom Hajninak, hogy mindig mellettem állt és támogatot.

Acknowledgments

I am in dept to my supervisor Prof. Ferenc Simon for introducing me to the world of experimental physics. I am grateful to him for all the professional guiding that I have received all through these years. I thank Milan Negyedi for his help in optics and Julianna Palotás for preparing the samples that I worked with. I thank Bence Bernáth, Bence Márkus and Balázs Gyüre for discussions and their help in the field of microwave physics. I am grateful for Prof. Thomas Pichler from the University of Vienna and Dr. Ferenc Murányi for from the IT'IS foundation, for providing excellent possibilities as a summer student. I am grateful to Sándor Bacsa and Béla Horváth for providing excellent mechanical components, that were essential for my work. I thank Dr. Ferenc Fülöp for his help in the field of electronics. I am very gratefull to my parents for their tireless support and for teaching me how to love my work. Finally I am grateful to Hajni, as she always stood by myself and assured me of her support.

Financial support by the European Research Council Grant Nr. ERC-259374-Sylo is acknowledged.

1 Introduction and motivation

Raman spectroscopy

Optical spectroscopic methods are powerful tools to investigate single walled carbon nanotubes (SWCNTs). Among them Raman spectroscopy is a widespread technique to investigate the electronic and vibrational proprties of SWCNTs. Technically two distinct approaches exist: the dispersive based one, where the spectral lines are spatially resolved and the Fourier Transform method, where the spectral lines are identified from there interference pattern. Historically, dispersive spectrometers were developed first with single-channel photomultiplier (PMT) detectors [1],where scattered photons for a single wavelength are measured. The development of charge coupled device (CCD)-based multichannel detectors for visible light operation substantially improved the sensitivity of dispersive spectrometers as therein many wavelengths are measured simultaneously. It is now generally accepted that CCD-based dispersive spectrometers are the best choice for visible Raman spectroscopy. The FT method was developed as late as 1986 despite the fact, that the technology for such development already existed in the 1970's. The Reason for that is the following: Raman measurements in the visible regime are limited by the shot noise of the signal. Under such circumstances the FT method shows a significant degradation of the Signal to Noise ration (SNR). However, Chase and Hirschfeld [2] [3] recognized that the main disadvantage of Raman spectroscopy in the visible regime, is that the weak Raman peaks are located on a strong photoluminescence (PL) background that hinders their detection. To get rid of the PL background, one must use a near infrared laser and detectors. However, such detectors are thermal noise limited and this is exactly where the FT method is superior to the visible method.
It is generally accepted that the dispersive method is only viable in the visible (VIS) regime, whereas the FT spectroscopy is only viable in the Near Infrared band (NIR), thus these two methods are considered as complementary techniques. It is considered as a futile approach to expand the FT technique to the VIS regime because there the Signal to Noise Ratio (SNR) is severely degraded due to the different nature of the noise [4–8]. Extending the FT-Raman spectrometer operation to the visible range would be of great advantage due to the $1/\lambda^4$ wavelength dependence of the Raman process [9]. In addition, the FT-Raman operation has several other advantages compared with the dispersive discussed in section Sec.2.4.3.
In this thesis, I present the development of an FT-Raman spectrometer working with a visible laser excitation. I show that when Raman spectroscopy is considered, the FT method not only does not suffer from SNR degradation but outperforms dispersive based ones when the laser power density is considered. These results were published in Ref.[10].

Photoluminescence spectroscopy

Photoluminescence (PL) spectroscopy is one of the most suitable techniques to investigate the electronic and optical properties of specific CNTs Ref.WangHeinz. Due to the quasi 1D electronic structure of the CNTs, the excited electron-hole system forms a strongly bound quasi-particle called *exciton*. Excitons are usually formed in a singlet spin state, however, due to spin-orbit interaction (SOI), there is a low probability of excitons being in a spin triplet. Such with spin triplet configuration hinders the efficiency of SWCNT based opto-electronic devices, as a recombination to to the ground state (that has singlet configuration) is spin-forbidden, i.e. triplet excitonic states form a metastable excited state. Little is known about the physics of SWCNT excitons in the triplet state, thus investigation of its electronic and magnetic properties is an important task to understand the mechanism underlying the formation of triplet excitons, and their decay rates to the groundstate. An Optically Detected Magnetic Resonance (ODMR) spectrometer - utilizing a dispersive spectrograph- was developed in our laboratory to investigate the aforementioned triplet states of SWCNT excitons [11]. This technique basically measures the very weak change of the PL lines of SWCNTs. This technically means coupling a PL spectrometer (Optically detected) to a magnetic resonance setup. The ODMR response of the SWCNT samples lay in the NIR regime 800-1500 nm and it is generally 3 orders of magnitude weaker than the PL response. However, measuring weak intensity signals in the NIR regime was the main reason why the FT-IR method was developed [2] [3], i.e. it seems straight forward step, to extend our ODMR measurements to the FT principle. However, developing an FT-PL spectrometer is the first step towards this goal.

In the second part of this thesis, I present the development of a FT-PL spectrometer working in the NIR regime. I discuss the technical realization of such setup, and the limits of its sensitivity. Finally I critically compare the constructed FT-PL spectrometer to the existing dispersive one.

2 Theoretical background

2.1 Fundamentals of Carbon nanotubes

Structure and Geometry

Carbon nanotubes (CNTs) can be considered as virtually rolled up graphene sheets. Interestingly the way it is ”rolled up” influences its electronic, optical and vibrational properties [13].

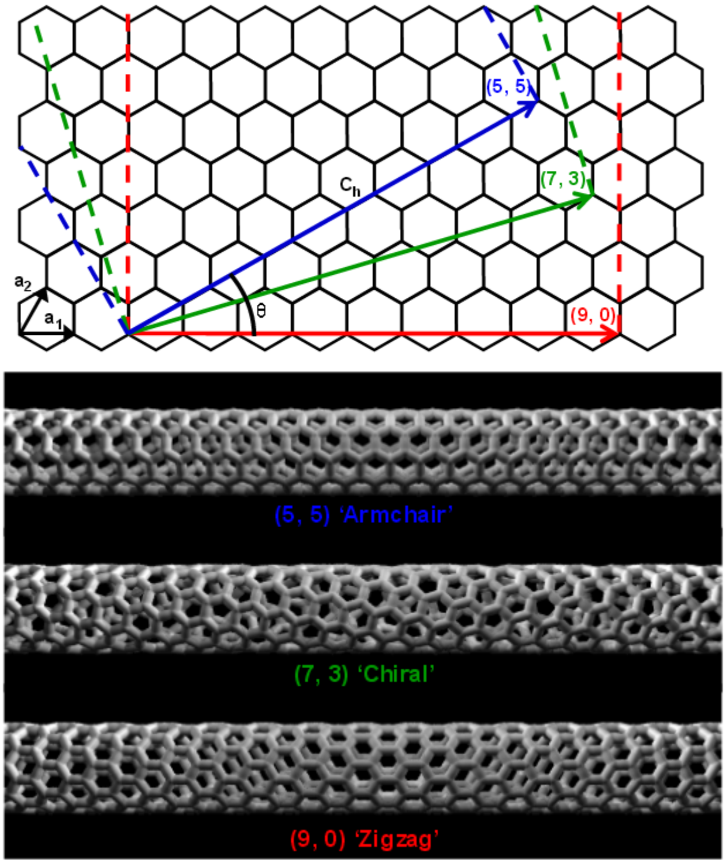

Figure 1: Top: The chirality vector (continuous line) C_h defined on a graphene sheet for *zig-zag* (red), *armchair* (blue) and arbitrary or *chiral* (green). Bottom: the corresponding nanotubes after ”rolling up”. Figure from Ref.[14]

The defining quantity of CNTs geometry is the so-called *chirality* that determines the unit-cell of the CNT. Chirality is defined as a 2D vector, along that the graphene sheet is cut and rolled up, thus it defines the circumference of the CNTs. In Fig.1 the chirality vector C_h is defined as the continuous arrows and described by coordinates (n, m). According to the values of (n, m), the geometry at the end of the tubes can show different patterns: an *armchair* pattern occurs when $n = m$, *zig-zag* when $m = 0$ and *chiral* otherwise. The chirality of the CNTs is directly related to the diameter of the nanotubes, whenre a_0 is the length if the graphene unit vector.:

$$d = \frac{a_0}{\pi}\sqrt{n^2 + m^2 + nm} \tag{1}$$

Electrical and optical properties of CNTs

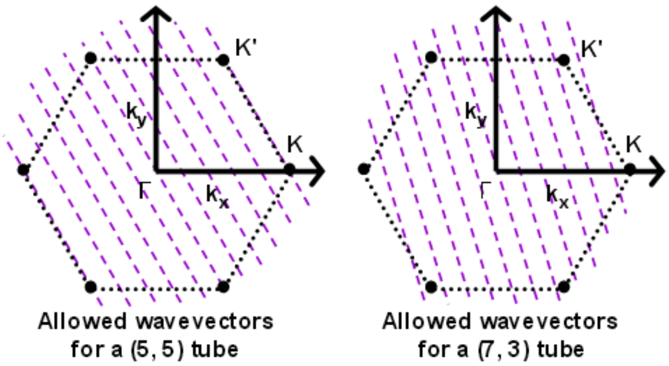

Figure 2: The cutting lines of CNTs superimposed on the graphene Brillouin zone. For CNTs with (5,5) chirality, the cutting lines includes the K and K' points of the graphene Brillouin zone, thus they are metallic. Contrary to this, (7,3) CNTs are semiconducting as their cutting lines excludes the K and K' points. Figure from Ref.[14].

It is known that the electron dispersion of graphene forms a continuous function in the corresponding 1st Brillouin zone. However, Rolling up the graphene sheet along the C_h vector imposes a periodic azimuthal boundary condition on the electron wave function. This defines "cutting lines" in the graphene Brillouin zone, along which those electronic states exist, which satisfies these boundary conditions i.e. the electronic structure is quantized in the azimuth degree of freedom and quasi-continuous only along the direction parallel to the CNT axis Fig2.

The quantum confinement in CNTs results a quasi 1D electronic dispersion, due to which so-called *Van Hoove* singularities are observed in the electronic DOS Fig.3. Depending on whether these cutting lines include the K and K' points of the original graphene Brillouin zone (where the conduction and valance bands meet), CNTs can be either semiconducting with a few eV bandgap, or metallic. Metallicity of CNTs occurs when the C_h vectors satisfies the $(m - n)\, mod\, 3 = 0$ relation Fig.3.

Optical properties of Carbon nanotubes

The optical properties of CNTs are also strongly affected by the presence of the Van Hoove singularities. Due to the quantized states of electrons along the circumference of the CNTs, they form sub-bands with well defined angular momentum. This in turn introduces selection rules for the interaction of light, as light can transfer angular momentum of $m = 0, \pm 1$ (depending on the polarization) when single photon scattering is considered. Also $|\Delta m| > 1$ can occur, however this would correspond to a two photon scattering, which

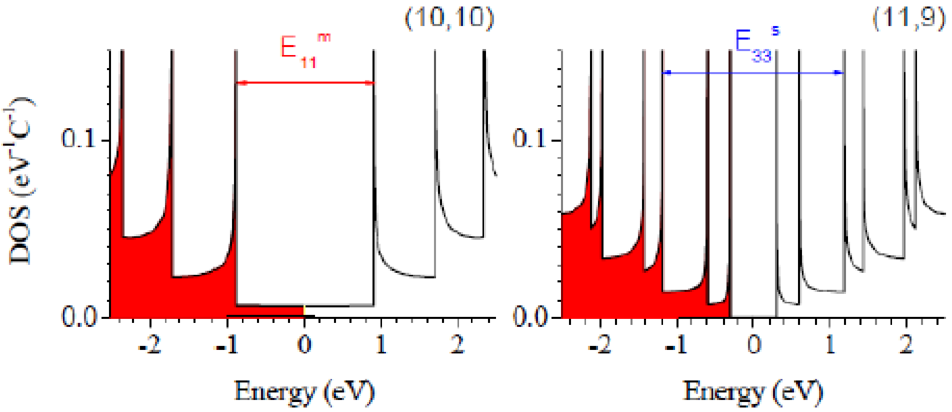

Figure 3: Van Hoove singularities in the CNTs DOS for metallic (left) and semiconducting tubes (right). Source Ref.[15]

is highly improbable relative to the single photon excitation, except for highly intense laser excitation. Because of the high DOS, electronic transitions are strong between the Van Hoove singularities. These transitions are symmetrically numbered corresponding to their distance from the Fermi level i.e. Electronic transitions can occur between the i-th Van Hoove band of the valence band to the j-th one in the conduction band, which is denoted by E_{ij}.

When the light is polarized along the CNT axis, the angular momentum transfer is zero $\Delta m = 0$, and only electronic excitation corresponding to "symmetrical" Van Hoove singularities can occur i.e. only E_{ii} type see 3. Electronic transition describing an $E_{ii\pm1}$, can also happen when the light is polarized perpendicular to the CNT axis, however, the probability of this kind of process is again low due to the so-called *antenna effect*: when an external **E** field is introduced perpendicular to the tube axis, it also induces charge-density along the wall, which in turn screens the external field, so that an $E_{ii\pm1}$ type transition is weakened.

The character of the excited CNT system also differs from that of conventional bulk materials due to the quasi 1D electronic structure of the CNTs. In a 3D semiconductors, an optically excited electron-hole pair is usually regarded as two independent particles, that are described by a delocalized wave function. However, this excited electron-hole system can also form a localized quasi-particle, due to the Coulomb interaction between them and they can be treated quantum mechanically in analogy to the hydrogen atom. Such quasi-particles formed by an electron-hole pair are called *exciton*. However, due to the Coulomb screening in these materials the binding energy of such excitons is typically in the order of 10 meV and thus they can not be detected at room temperature but rather requires cryogenic temperatures to be observed. An example from Ref.[16] is shown in Fig.4.

Due to the 1D structure of CNTs, the Coulomb screening is much weaker than in 3D semiconductors, as charge density (and screening) can only change along the tube axis, thus the exciton binding energies are much higher in the order of 0.5 eV. An other interesting feature in CNTs is the so-called *Exciton Energy Transfer* or EET: CNTs are characterized by a strong sp^2 bond of the carbon atoms along the wall, but also due to the

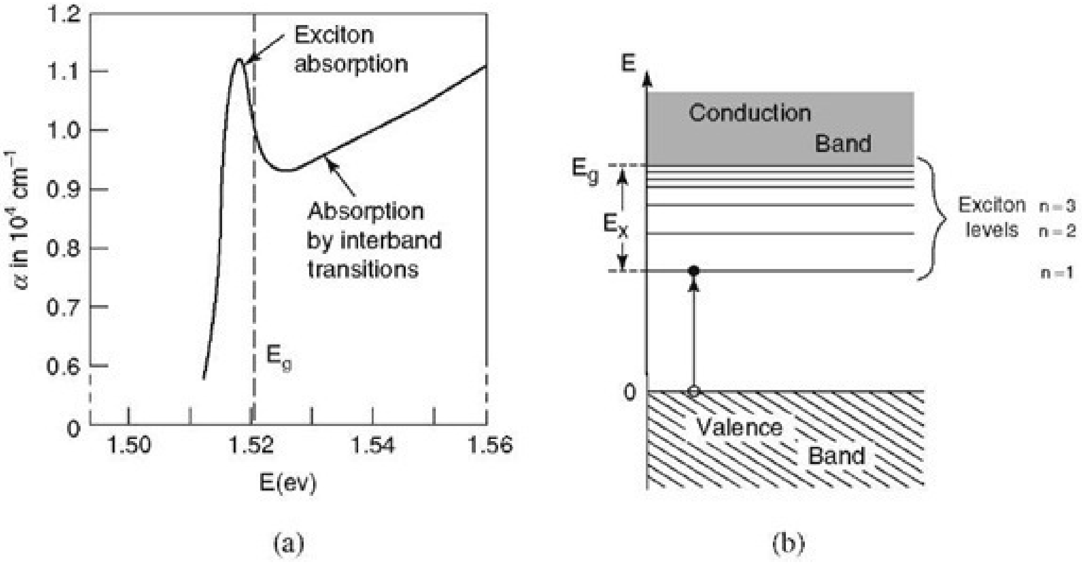

Figure 4: a):Optical absorption of GaP single crystal at 21K. A peak corresponding to exciton excitation appears at energies below the band gap.b): The corresponding energy structure of the material: at low temperatures quantized energy levels appear just below the gap energy corresponding to weakly bound excitons. Figure from Ref.[16]

weak van der Waals-force, separate tubes will attract each other forming a hexagonally arranged close packed geometry. The same is observed in graphite, where strongly bonded graphene sheets are weakly bonded together by the van der Waals-force forming the known stacking structure of graphite. When an exciton is formed on one CNT, it can "jump" to a neighboring "acceptor" tube, provided there is a resonant channel between the two tubes (the edge of the conduction band is higher in the host). If such EET occurs, the emission of a photon (due to the exciton decay) has a photon energy corresponding to the acceptor CNT band-gap see Fig.5, these are the *bundle peaks*.

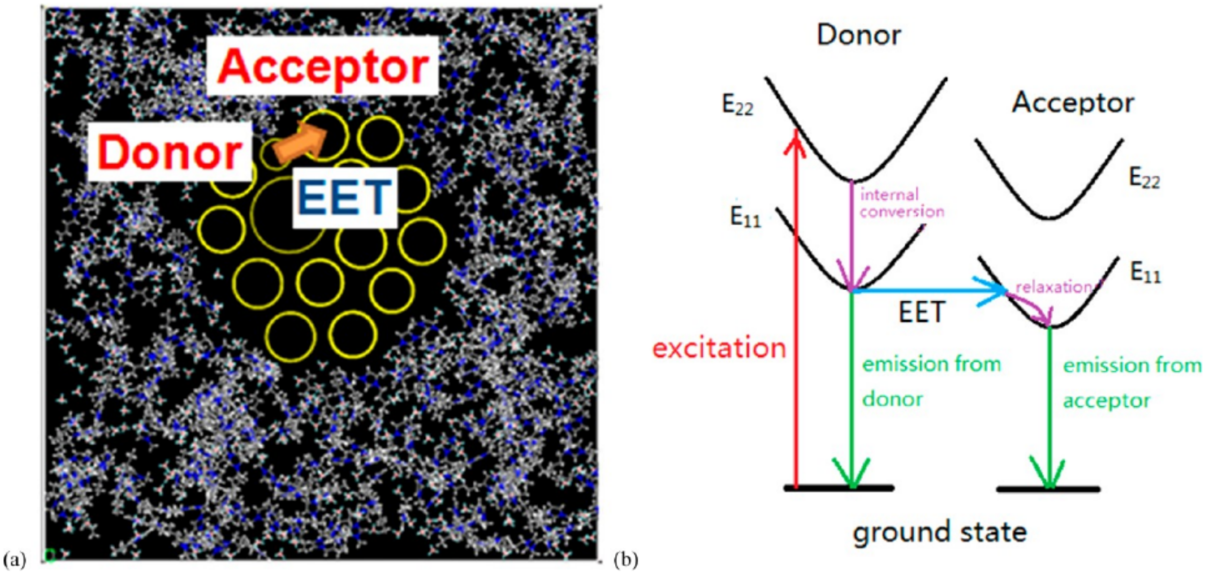

Figure 5: EET mechanism in bundeled CNTs. An exciton formed in the donor tube will relax to the lowest possible energy state (purple arrow), from which it decays by a photon emission (green arrow). In case where CNTs are bundled, excitons can be transferred to the neighboring acceptor tube. In this case exciton decay occurs by an emission of a photon of a lower energy than the donor band gap [17].

2.2 Photoluminescence

Luminescence is the process when an excited electronic state decays by the emission of light. Photoluminescence is the process when the energy transfer happens with light irradiation. Further we distinguish Fluorescence and Phosphorescence radiation depending on the lifetime of the excited state: Fluorescence is a very fast process, whereas in the case of Phosphorescence radiation, the excited states is a metastable state, thus the relaxation time is much longer. Before going into details of the photoluminescence process of CNTs, I discuss the different spin states of an exciton. As excitons are composed of an electron-hole pair, they posses a total quantum angular momentum of $l = l_1 + l_2$ where $l_i = 1/2$. According to the l quantum number value they are either in ψ_S singlet state $l = 0, m = 0$, or a ψ_T triplet state $l = 1, m = 0, \pm 1$.

$$\begin{aligned} \psi_S &= \frac{1}{\sqrt{2}}(|\uparrow\downarrow> - |\downarrow\uparrow>) \\ \\ \psi_T &= \frac{1}{\sqrt{2}}(|\uparrow\downarrow> + |\downarrow\uparrow>) \\ \psi_T &= |\uparrow\uparrow> \\ \psi_T &= |\downarrow\downarrow> \end{aligned} \tag{2}$$

These types of states play an important role in the photo physics of CNTs, as a transition between a singlet to a triplet (and vice versa) is forbidden in the first order.

The photoluminescne process is schematically described in Fig.8. Depending on which

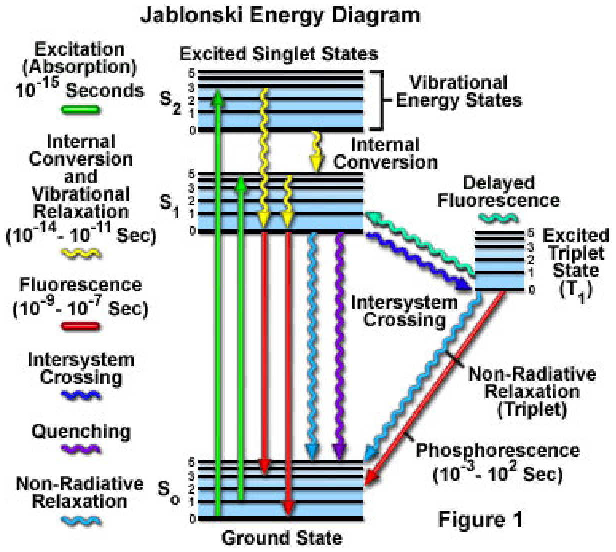

Figure 6: The Jablonski diagram of photoluminescence process along with the typical timescales for the various processes . Figure from Ref.[18].

electronic state is excited, excitons are formed in a singlet state and are denoted with S_i. In our case S_1 denotes the singlet state of E_{11} excitation and S_2 that of E_{22} in Fig.3. Note that theses energy states are not well defined, as they are superimposed on a continuous vibrational sub-levels. As the transition time between these sub-levels (vibrational relaxation) is much shorter than the typical timescale of the Fluorescence process, the excited exciton rapidly relaxes to the bottom of the of the band-gap by emission of phonons. This is exactly why metallic CNTs do not show luminescence activity. Generally a transition between S_1 and T_1 is forbidden as light cannot induce a spin changing transition. However, in case of CNTs, the presence of a weak spin-orbit coupling violates this symmetry and a transition between S_1 and T_1 can occur with a low probability. This is called *Inter System Crossing*. Also the population of the three T_1 sub-levels is not necessary equal. This is due to the different symmetry of the electronic wavefunction, i.e. the coupling SOC matrix element (and with it the transition probability) is different for each m sublevel of T_1. As the ground state of the excitons is always a singlet S_0, the T_1 state is a metastable state, described by a very long radiative relaxation (Phosphorescence) time, 4 orders longer than that of S_1.

Optically detected magnetic resonance

ODMR is hybrid method that combines the techniques of microwave Electron Spin Resonancy (ESR) with photoluminescence. It includes both the high energy resolution of microwave spectroscopy and the high sensitivity of optical spectroscopy. The basic concept of ODMR is to detect the change of the PL intensity (optical detection) by changing the population of the T_1 sublevels using microwave excitation (magnetic resonance). This method is suitable to investigate the physics of these metastable T_1 sublevels, as e.g. their lifetime, interaction strength etc.

The general Jablonski diagram of the ODMR process is shown in Fig.7. The SOI couples differently to the T_3 sublevels, i.e. the ISC k_{ISC} rate is different also, resulting

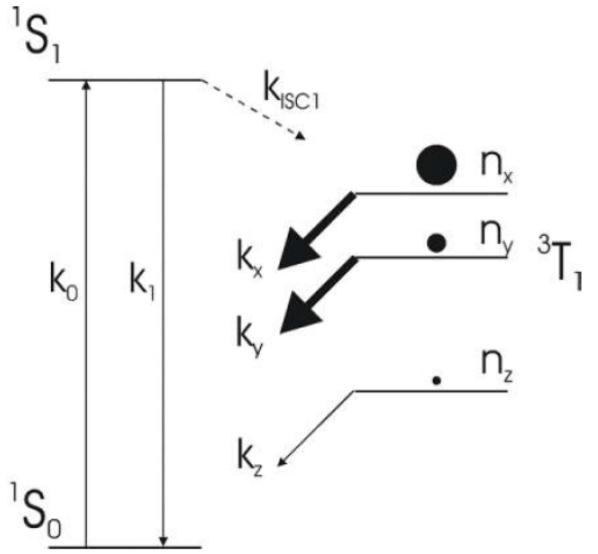

Figure 7: The Jablonski diagram of the ODMR process. Different dot sizes on the T_3 sublevels indicate different population, while different arrow widths indicate different relaxation rates. Figure from Ref.[11]

in a different value of populations (n_x, n_y, n_z). Also note that the transition rates to the S_0 groundstate (k_x, k_y, k_z) for these sublevels differ also. By altering the population (n_x, n_y, n_z), the net rate of the luminescence is also changed. For example sublevel z has a transition rate k_z smaller then the other two sublevels, thus if the population n_z is increased, it quenches those excitons that would otherwise participate in the PL process, i.e. the amplitude of the PL process will decrease. In an ODMR experiment the CNT sample is put in a magnetic field so the T_3 sublevels are split. By applying a microwave radiation maching the energy difference between two such sublevels, the distribution of the population and with it the PL intensity will change. However, there is an important criteria for a long standing and significant change of population, namely that these microwave transition should be able to be saturated (i.e. an inversion of population is maintained). This means that the spin relaxation time T_1^{spin} (not to be confused with T_1, that only denotes the triplet spin state of the excitation) should be very large. If T_1^{spin} is short, then the excited electrons between the T_1 sublevels would decay fast and the population of the three T_1 sublevels would be always equal to that of the thermal equilibrium, i.e. no longstanding change of the sublevel population is achieved and no change in the PL intensity is detected.

The change of the PL intensity due to the population change of the T_1 sublevels is very weak typically 10^{-3} for CNTs. Experimentally this means that we want to detect a small change of an otherwise intense PL lines. Generally this type of direct measurement is hopeless as this weak effect would be buried in the noise of the measurement, thus it is necessary to apply Lockin techniques to separate in amplify the weak effect from the intense noisy background.

2.3 Raman scattering

Raman spectroscopy - named after Sir C. V. Raman (Nobel Prize 1930) who discovered this technique [12] - is a non destructive optical method, applied in a wide range of scientific fields like physics, chemistry, and biology. This technique relies on detecting the vibrational response of the specimen and it is an outstanding tool when investigating such important properties as the purity, electronic, and vibrational states of carbon nanostructures. The reason why Raman spectrosscopy is useful lies in the fact that carbon nanostructures lack dipolemomentum due to the monoatomic construction, therefore they do not possess infrared active modes. This makes Raman spectroscopy the only feasible method to study their vibrational properties.

Raman scattering is a type of inelastic photon scattering, where energy is transferred to or from the crystal, due to the creation or decay of phonon modes in the solid (or vibration modes of molecules). The physical process underlying this effect is the following: a photon with arbitrary energy (in the visible or infra-red range) absorbed by an electron of the solid excites the electron to a virtual state, after which it relaxes by both emitting a phonon and a photon (Stokes Raman process), thus introducing a phonon to the solid, see Fig. 8. Relaxation of the electron can happen also by further absorbing a phonon while in the excited virtual state, after which photon emission occurs, in the end a phonon mode is destroyed in the solid (Anti-Stokes Raman process) The process is sketched in Fig.8. By adjusting the incoming photon energy to match the transition energy of two real electronic states of the system, the probability of Stokes-Raman scattering can be enhanced by several orders of magnitude (up to 10,000x factor), which makes it possible to detect single molecules (resonance Raman scattering). For instance this type of scattering is highly applicable to carbon based nano-materials as graphene and graphite.

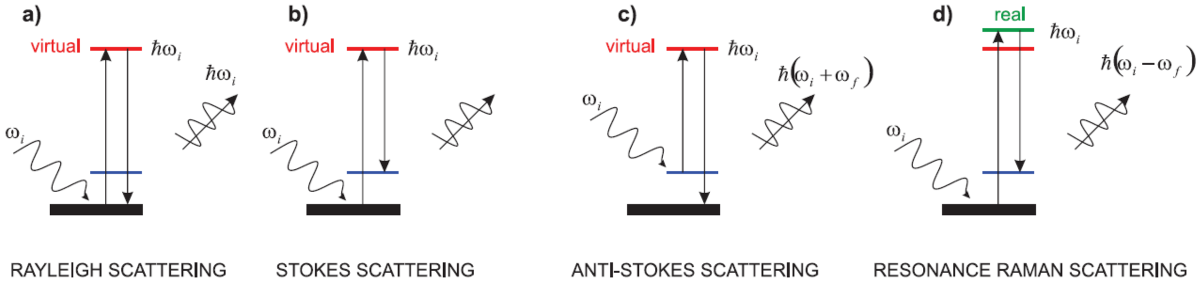

Figure 8: Energy diagram of the possible scattering processes: Stokes process results in the emission of a phonon thus the scattered light is red-shifted. Anti-Stokes process results in the absorption of a phonon, thus the scattered photon is blue-shifted. Resonant stokes occurs when incoming photon energy matches that of an electronic transition. ω_i denotes the angular frequency of the incoming photon, while ω_f that of the phonon Ref.[19]

The governing equations of Stokes Raman scattering can be introduced by applying conservation of energy and momentum:

$$\begin{aligned} \hbar\omega_i &= \hbar\omega_s + \hbar\Omega \\ \hbar k_i &= \hbar k_s + \hbar q \end{aligned} \tag{3}$$

Where ω_i (k_i) is the angular frequency (wave number) of the incident-, ω_s (k_s) of the scattered photon, Ω (q) is the angular frequency (wavenumber) of the emitted phonon. Equations (3) yields a linear dispersion $p_{phonon} = cq$ where c is the speed of light, phonon modes must also obey their dispersion relation in the solid, so because the immense slope of the linear dispersion phonon modes only around the Γ point $(q = 0)$ of the first Brillouin zone will be available for Raman scattering see Fig. 9. Conservation of energy and

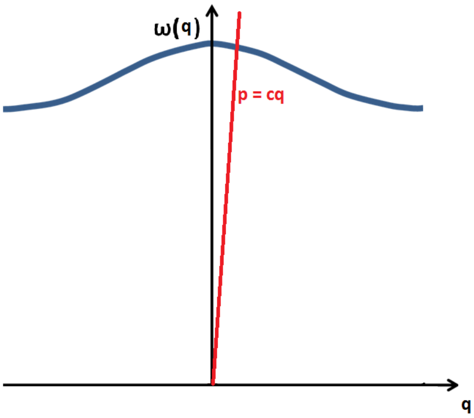

Figure 9: Phonon modes available for Raman scattering. Created phonons have impulse equivalent where the linear dispersion intersects the phonon dispersion

momentum is not enough to understand the Raman spectrum, as the scattering process must obey selection rules: a phonon modes is Raman active if the derivative of the polarizability with respect to the spatial coordinates is non zero around the equilibrium point [9].

2.4 Fourier Transform spectroscopy

As I have already discussed, the ODMR signal of SWCNTs is 10^3 times weaker than the PL response, thus it is critical to operate our measurement setup at the lowest noise floor possible. To achieve this, one must understand the experimental techniques applied in the optical spectroscopy from the view point of excitation, light collection, spectral resolution and light detection. Special attention should be payed to the various noise sources in a spectroscopic measurement as it determines the method to be used. Basically two major techniques exist in the field of optical spectroscopy Fig. 10: The dispersive technique is used when the optical response lay in the UV or visible regime: the scattered light from the sample is guided to a diffraction (or optical) grating, from where light components with different wavelengths are dispersed to a single channel photodiode or a multi-channel CCD camera.

The *Fourier Transform* (or FT) technique is viable when the optical response lay in the infrared (IR) or the THz regime [9] for reasons to be discussed later in this chapter, Sec.2.4.3. Contrary to the dispersive technique where the core phenomena is the diffraction of light, here the spectral resolution is achieved by the interference of light: the scattered light is guided through an interferometer (typically Michelson interferometer). The periodic, decaying interference pattern is recorded in the time domain from which the spectrum is acquired by applying a Fast-Fourier-Transformation (FFT) [20].

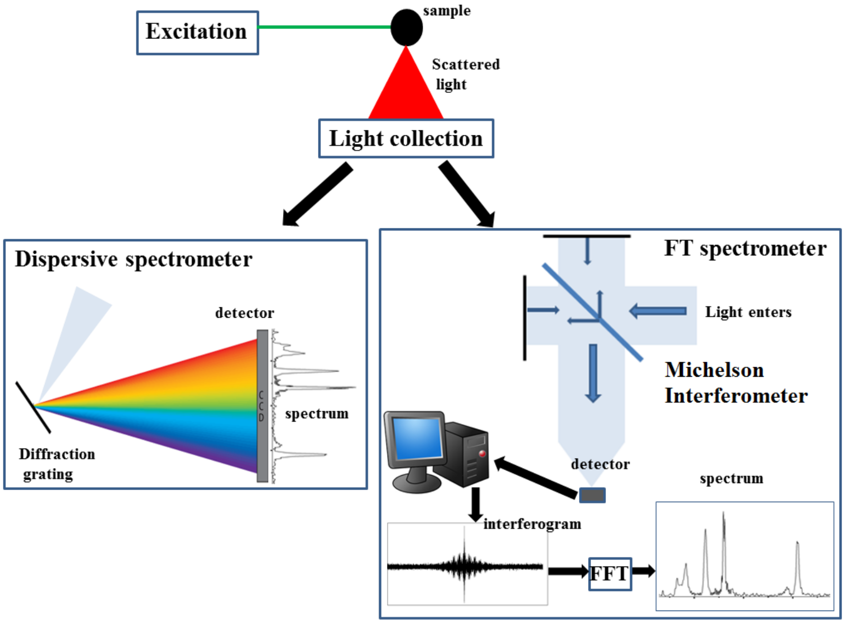

Figure 10: Schematic representation of dispersive and FT optical spectroscopy

2.4.1 The interferogram and sampling

Interference of light occurs when two monochromatic light waves are present in the same space, and thus they are superimposed in a phase correct manner. Suppose that there is a δ phase shift between the two waves, introduced by the Michelson interferometer

Eq.(4).

$$\begin{aligned}\underline{E}_1 &= \underline{E}_o e^{i(\underline{k}\,\underline{r}-\omega t)}\\ \underline{E}_2 &= \underline{E}_o e^{i(\underline{k}\,\underline{r}-\omega t+\delta)}\end{aligned} \tag{4}$$

The detected intensity at the exit of the spectrometer is proportional to the square value of the absolute value of the electric field, which after a brief calculation can be brought to the following form:

$$I \propto |\underline{E}_1 + \underline{E}_2|^2 = 2E_0^2(1+\cos\delta) \tag{5}$$

In a Michelson interferometer the relative phase shift between the two traveling waves is achieved by introducing a time dependent Optical Path Difference or OPD ie.

$$\delta = \mathrm{OPD}\,(t)\cdot\frac{2\pi}{\lambda} = k\cdot\mathrm{OPD} = k\cdot v_{mir}t \tag{6}$$

The light beam traveling in one arm of the interferometer travels somewhat longer or shorter distance compared to the other arm. Technically this means that one mirror of the interferometer is held fix, while the other one is swept with uniform velocity v_{mir} typically for about 1 cm long distance Fig.11(a). By varying the OPD, one can change the δ phase difference Eq.(6), where λ is the wavelength of the radiation and k is the wavenumber. The minimum places of the periodic time dependent signal will be separated by $\frac{\lambda}{v_{\mathrm{mirror}}}$ in the time domain, ie. the periodicity is unique for every wavelength. In case of $\mathrm{OPD} = n\lambda$ there is a constructive interference, and for $\mathrm{OPD} = (2n+1)\frac{\lambda}{2}$ there is a destructive interference Fig.11(b).

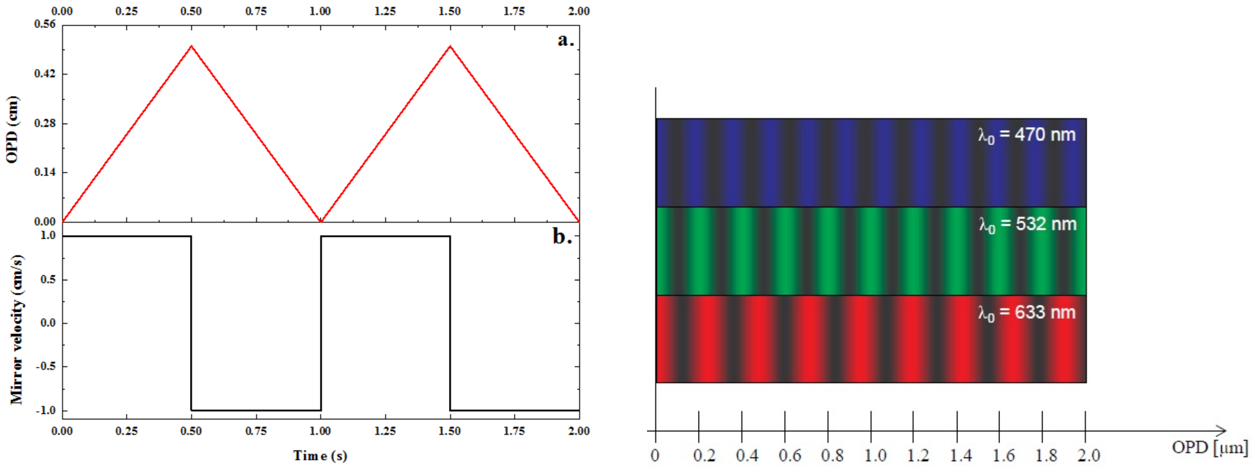

(a) Picture 1

(b) Picture 2

Figure 11: Fig. a: typical velocity of the moving mirror along with the time dependent OPD. Fig. b: Depending on the OPD the periodicity of the interference pattern is unique for each wavelength

Generally the scattered light is not monochromatic but rather has a wavenumber dependent intensity (spectrum) $E(k)$. According to Eq. (5) the interference (at a given mirror position x) of the spectral components between wavenumbers k and $k+dk$ is

$dI(k,x) = 2E(k)(1+\cos kx)dk$. To get the total detected intensity at mirror position x we have to integrate with respect to the wavenumber variable:

$$I(x) = \int_{-\infty}^{\infty} 2E(k)(1+\cos kx)dk \tag{7}$$

By removing the offset (this can always be done) we get that the detected intensity: the *interferogram* is the inverse Fourier transform of the spectrum, thus by applying an FFT algorithm we can acquire the spectrum directly Eq.(8).

$$\begin{aligned} I(x) &= Re\{\int_{-\infty}^{\infty} 2E(k)e^{ikx}dk\} \\ E(k) &= Re\{\frac{1}{2}\int_{-\infty}^{\infty} I(x)e^{-ikx}dx\} \end{aligned} \tag{8}$$

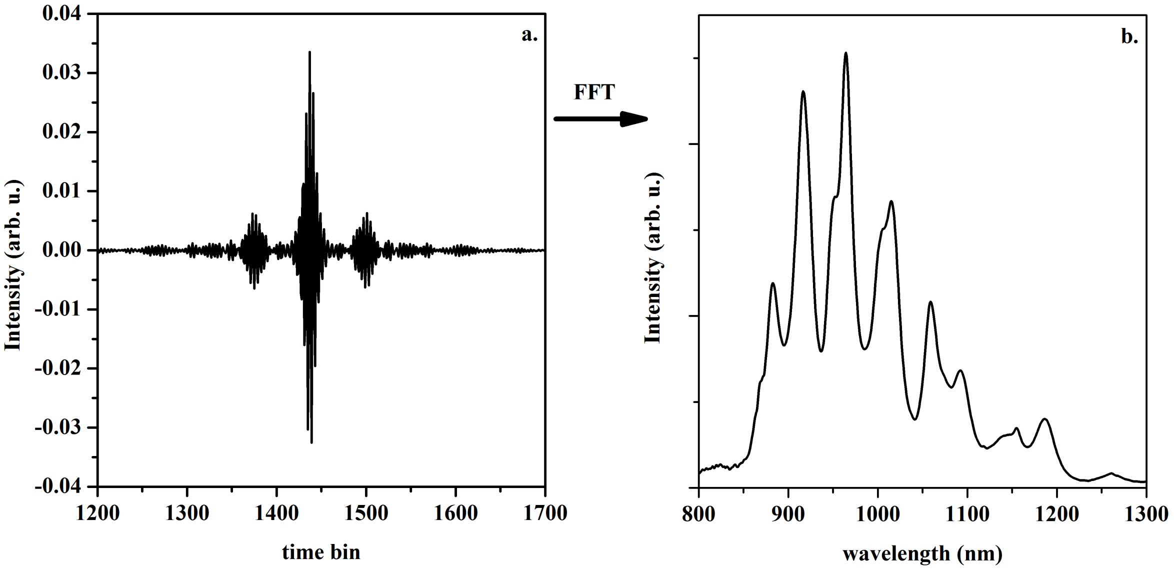

Figure 12: a) typical exponentially decaying interferogram of a broad band source (PL lines of SWCNT). b) A FT of the interferogram yields the spectrum

The sampling

One of the key features in FT-spectroscopy is the sampling mechanism. Every FT-spectrometer is equipped with a so-called reference laser, which is usually a highly coherent He-Ne laser lasing at 633 nm. The unknown wavelength of the scattering light is measured in the units of the He-Ne wavelength, i.e. the scattered light is calibrated with respect to the He-Ne as a known standard. The schematics of this concept is shown Fig.13: The interference pattern of the He-Ne laser is recorded with a separate detector, which serves as a sampling frequency for the main detector's electronics (that detects the scattered light), i.e. each time the He-Ne detector signal drops to zero, the main one takes a measurement point Fig.13. This sampling frequency can be usually set in the measurement software. In our case e.g. it is set to 1 kHz, thus the moving mirror is swept with such v_{mir} velocity that the He-Ne interferogram time constant is 1 ms. This is regarded as the reference value. For example if the interferogram contains a signal that has a time constant $T = 5T_{\text{He-Ne}} = 5ms$ than it is assigned to a wavelength $\lambda = 5 \cdot 633 = 3165\,\text{nm}$.

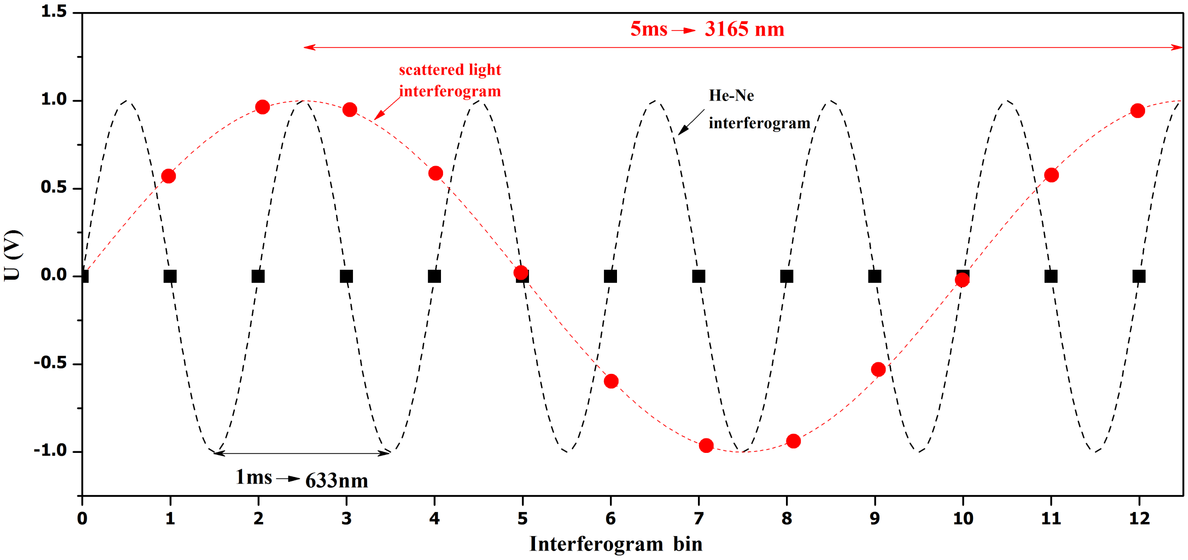

Figure 13: Sampling mechanism of a FT-spectrometer. Dashed black is the time dependent intensity of the He-Ne according Eq. (5). The black measurement point serves as a control signal to control both the mirror velocity and the sampling frequency. The interferogram of the scattered radiation (red dashed curve) is then sampled at these points, and compared to the frequency of the He-Ne laser (the standard).

2.4.2 The resolution

In FT spectroscopy the resolution is mainly determined by the maximum path length of the moving mirror or the maximum of the OPD [21]. Suppose we want to measure the wavelength of an infinitely coherent light that has a Dirac delta spectra centered at some f_0 frequency. The interference pattern is then a cosine function Eq.(5), that extends to infinity Fig.14. However, in a real measurement we have a finite measurement time T, which can be mathematically considered by multiplying the ”infinite” cosine function with a *Boxcar* or *Rect* function which assumes the value 1 during the measurement time and zero otherwise. This phenomenon is also called *apodization*. The effect of this truncation will manifest in the resolution as a broadened line according to Eq.(10) where $I(t)$ is the time dependent interferogram, The T subscript denotes the truncated signal, and $\mathscr{F}$ denotes the Fourier transformation. This means that if we define the resolution as the Full Width at Half Maximum of the peak than this FWHM scales as 1/T, thus the longer we measure the better is the resolution. Given that the moving mirror velocity is constant this means that the bigger is the OPD_{max} the better is the resolution.

$$\begin{aligned} I(t) &= cos(f_0 t) \\ I_T(t) &= Rect(t) \cdot cos(f_0 t) \\ \mathscr{F}\{I_T(t)\} &= 2T\frac{sin((f-f_0)T)}{(f-f_0)T} \\ FWHM &= \frac{1.21}{2T} \end{aligned} \tag{9}$$

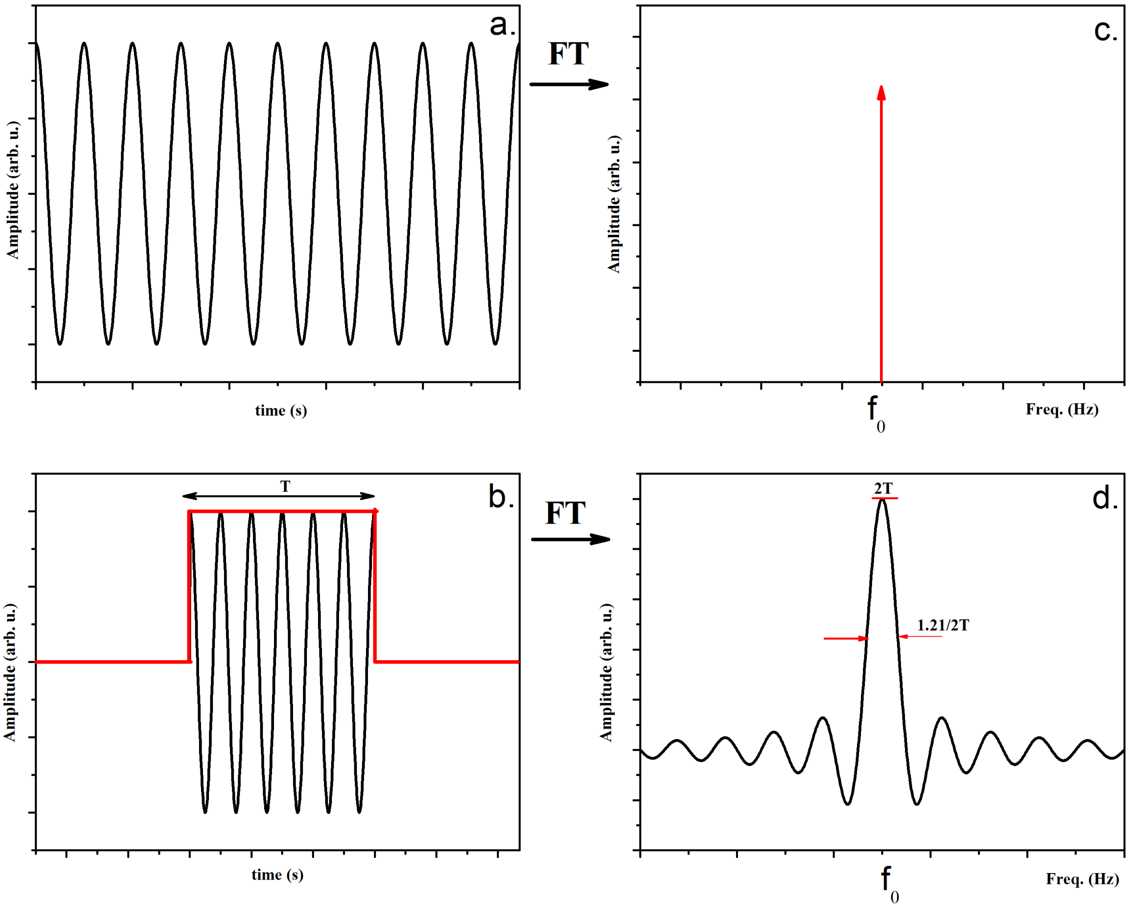

Figure 14: The interferogram of an infinitely coherent light is a cosine function (fig. a.) with a spectrum (Fourier transform) of a Dirac delta centered at a frequency f_0. However, the finite measurement time can be modeled as a truncated signal (fig. b.), that have a spectrum of a broadened *sinc* function.

To get better accustomed to this concept, let us take real measurement with the following typical setups: sampling frequency $f_s = 5\,\text{kHz}$, wavenumber resolution $\delta k = 4\,\text{cm}^{-1}$. Now as the Reference He-Ne wavenumber 15797 cm^{-1} corresponds to 5 kHz, then $4cm^{-1}$ resolution will correspond to 1.266 Hz frequency resolution. From the FWHM Eq.(10) we get that the measurement time should be $T = 2.1s$. Knowing that the mirror velocity is $v_{mir} = \frac{633nm}{200\mu s} = 3.15mm/s$, this translates to total pathlength of 6 mm i.e.

OPD$_{max}$ of 3 mm. Again if we want $\delta k = 1 cm^{-1}$ we get that OPD max = 1.2 cm. Thus the rule of thumb is: to achieve 1 cm^{-1} resolution we have to scan 1 cm long OPD$_{max}$ [21].

$$\delta k = \frac{1}{\mathrm{OPD}_{\mathrm{max}}} \tag{10}$$

The question naturally arises: what is the limiting resolution of the instrument if the only thing we have to do to increase it, is to increase the path length of the moving mirror? Up until know we assumed that the beam entering the interferometer is completely collimated and parallel. However, this is not the case in reality, as the beam will always have an angular divergence to some extent which limits the resolution. Further, this divergence of the beam is directly caused by the size of the irradiated area of the sample, i.e. the size of the focus or aperture.

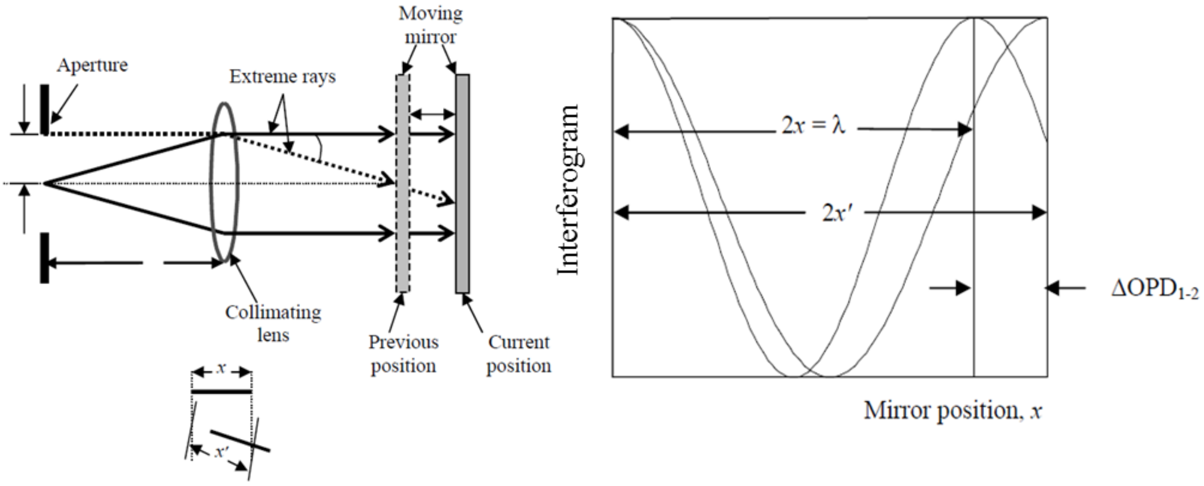

Figure 15: Schematics of the limiting resolution due to beam divergence from Ref.[[21]]

Again suppose we want to measure the wavelength of a monochromatic light that enters the interferometer. Due to the beam angular divergence, there will be rays that travel somewhat longer distances x' relative to collimated rays that travel distance x. The interferogram consisting of the superposition of a collimated-uncollimated ray will give a constructive interferogram at a differenct OPD$_2$ than that of a collimated-collimated one OPD$_1$, see Fig.15. If the difference in OPD$_1$ and OPD$_2$ i.e. ΔOPD $= \frac{\lambda}{2}$, than the two rays will be out of phase. This will be interpreted as if there is a spectral line of a finite amplitude near to the line λ that we want to measure i.e. the spectrum will be broadened, and the total resolution will be no longer determined by the the $\frac{1}{\mathrm{OPD}}$ rule from Eq.(10) (OPD limited), but rather divergence limited [21].

From a simple geometric consideration Fig.15 we find that $x' = \frac{x}{cos(\alpha)}$ where α is the angle between the two extreme rays. From here we can determine the $\Delta\mathrm{OPD} = |2(x' - x)| = |2x\left(\frac{1}{cos(\alpha)} - 1\right)|$. Using the small angle approximation $cos(\alpha) = 1 - \frac{\alpha^2}{2}$ gives $\Delta\mathrm{OPD} = x\alpha^2$. As mentioned before the uncertainty of the interferogram occurs at $\Delta\text{OPD} = \frac{\lambda}{2}$ which is clear for a monochromatic source, but how about a broadband source? There the divergence-limited resolution limit will be given by the shortest wavelength present in the spectrum, thus the criterium will be $\Delta\text{OP}D \leq \frac{\lambda_{\text{min}}}{2}$. Putting everything together yields:

$$\alpha^2 \leq \frac{1}{2xk_{max}} = \frac{1}{\text{OPD}_{\text{max}}k_{\text{max}}} = \frac{\delta k}{k_{\text{max}}} \tag{11}$$

Again from Fig.15 we can see that $\alpha = \frac{a}{f}$. As the focus length f of the collecting optics is usually fix, the only parameter that we can vary to fulfill Eq.(13) is the aperture stop a which is also called *Jacquinot stop.* By setting the desired resolution we also set the aperture-stop of the instrument.

$$a \leq f\sqrt{\frac{\delta k}{k_{max}}} \tag{12}$$

To quantify this property let us take a simple example with typical values:

$$\delta k = 4cm^{-1}, k_{max} = 9398cm^{-1}(1024nm), f = 2.5cm \tag{13}$$

This leads to a maximum aperture of $1000\mu m$ (diameter) which is far larger than a diffraction limited focus spot typically $1\mu m$ diameter.

2.4.3 Advantages of FT-spectroscopy

Fourier spectroscopy has several advantages when compared to dispersive spectrometers. In the following, I discuss the three main advantages, that led to the proliferation of the FT-IR optical spectroscopy.

Jacquinot advantage

The resolution of dispersive spectrometers is determined by the size of the entrance slit. However, for low resolution spectroscopy the entrance slit will be the defining aperture stop of the optical system, rather then the focus spot size on the sample. Due to this, we will lose a lot of photons on the spectrometer entrance i.e. the trade of here is: increasing the resolution decreases the signal. In case of FT-spectroscopy on the contrary the trade of is as follows: increasing the resolution increases the measurement time Eq.(10). A resolution down to $0.001cm^{-1}$ or $0.0001nm$ is commercially achievable [22], where as the typical values for dispersive spectrometers is $0.01nm$. This property, called *Jacquinot advantage*, is not only desirable but directly essential for some applications where the task is to measure low intensity narrow lines e.g. in quantum optics, atomic physics and cosmology all of where high energy resolution/ high optical throughput methods are required.

I demonstrate the *Jacquinot advantage* on two spectrometers that we have in our lab: a dispersive *Jobin Yvon iHR 320 single* single channel dispersive and a *Bruker IFS 66v* FT-spectrometer.

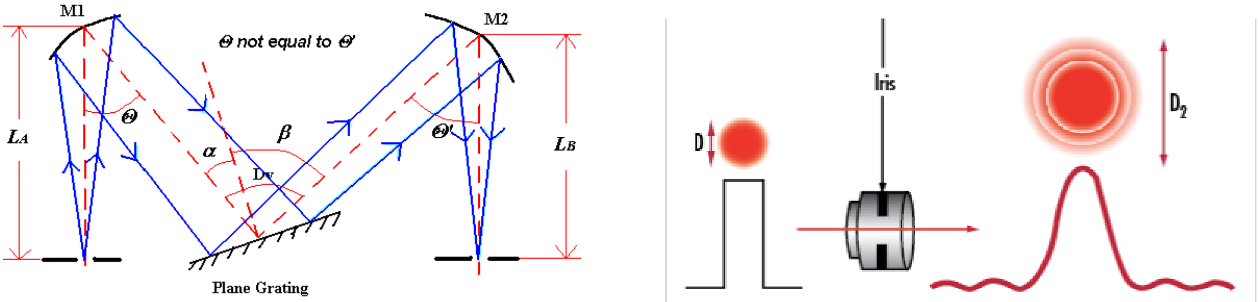

(a) Picture 1

(b) Picture 2

Figure 16: Left: typical spectrograph setup in a dispersive spectrometer, where the resolution is determined by the entrance slit width. Right: The *Airy* disk diffraction limited focus spot on the sample

The resolution of dispersive spectrometers is described by Eq.(14), where W is the slit width at the entrance (or exit) of the spectrometer, $\Delta\lambda$ is the desired wavelength resolution, k is the diffraction order, β and L_b are denoted in Fig.16(a) and n is the number of grooves/mm of the diffraction grating.

$$\Delta\lambda = W\frac{\cos\beta}{knL_b} \tag{14}$$

Substituting the typical values of our dispersive spectrometer :$k = 1, \beta = 30^o, n = 600\text{groove}/mm, L_b = 320mm$ in Eq.(14) yields $W = 20\mu m$ for the slit width, assuming a desired resolution of $1cm^{-1} = 0.1nm$. However the focus spot size is determined by the *Airy* disk diameter [23], and reads Eq.(15). For the so-called *Macro setup*, the diameter of the focusing lens is much larger than the diameter of the laser beam D, i.e. the effective f-number of the system is $f/D > 1$ and not $f/\sharp \cong 1$. Again substituting $\lambda = 1000nm$, $f = 2.54cm$ and $D = 3mm$ we get a diffraction limited spot size (diameter) of $d = 20\mu m$, thus if we want to improve the resolution by narrowing the slit we will lose photons at the entrance of the spectrometer. This effect can be counterweighted by applying a microscope lens e.g. by coupling the spectrometer to a microscope. In this case the effective f-number f/D will be equal to the nominal f-number $f/\sharp$ generally 1 for most microscopy objectives. Under theses circumstances the *Airy* disk of $2.44\mu m$ is much smaller than the entrance slit width and the throughput of the spectrometer is high again. However, note that by reducing the spot size (increasing the laser power density) one can easily achieve the power damage threshold of the sample.

$$\begin{gathered} d = 2.44\lambda\frac{f}{D} \;\; \text{for Macro setup} \\ d = 2.44\lambda\frac{f}{\sharp} \;\; \text{for Micro setup} \end{gathered} \tag{15}$$

In case of FT-spectrometers, no entrance slit is required for the resolution as discussed in Sec.2.4. However, a focusing of some degree is still required to avoid resolution degradation due to angular divergence Sec.2.4. According to Eq.(13), a focus spot radius of

$500\mu m$ is required for a $\delta k = 1cm^{-1}$ resolution, which is far larger than the diffraction limited focus spot size. This results in a much lower power density on the sample (compared to both dispersive micro or macro setup). The *Jacquinot* effect is presented in Table. 1.

	disp-macro setup	disp-micro setup	FT-setup
Focusing	intermediate	strong	weak
Focus size	$20\mu m$	2.44 μm	250 μm
Power density	320 W/cm^2	21.5 kW/cm^2	1 W/cm^2
SNR increment	65	1	10^4
Aperture stop	slit	focus	focus

Table 1: Summary of the Jacquinot effect taken for dispersive *Jobin Yvon iHR 320* dispersive spectrometer, assuming a focusing lens of f=2.54 cm and laser beam diameter D=3mm mm for the macro setup and $f/\sharp = 1$ for the micros setup. Power density is calculated for 1mW irradiation, that is a typical damage threshold in a micro-dispersive setup.

In the current case where either PL or ODMR spectra is measured, the natural linewidths are $10 - 20nm$. To measure such broad lines, even for a macro-dispersive channel the entrance slit can be set large. The limiting aperture is then be the focus spot and high optical throughput can be achieved again. It seems pointless to talk about the *Jacquinot* advantage in cases were no high resolution is required. However, the *Jacquinot* advantage has an other consequence: even if the resolution of dispersive spectrometers is not limited by the slit, it is still required that the exciting laser is focused on the sample, thus high power density is maintained, which can lead to heating effects that distorts the measured optical spectrum, or even damaging the sample. On the contrary such high power density is not maintained in case of FT-spectroscopy, as there no strong focusing is required. When the power of the irradiated laser reaches the sample's damage threshold ($1mW$ in case of micro-dispersive setup), further increase of the SNR is not possible. The true manifestation of the *Jacquinot* advantage in our case is the immense room (10^4) to increase the excitation power and with it the SNR, without reaching the damage thershold, as demonstrated in Table 1.

Fellgett advantage

The *Fellgett* advantage is the increased SNR of the spectrum measured in the frequency domain compared to that measured in the time domain [24]. Originally this was the leading reason of the proliferation of FT-spectroscopy where a weak signals are to be measured [2] [3].

The nature of the Fellgett advantage lays in the fundamental property that FT-spectroscopy is a multichannel method: By sweeping the moving mirror in the interferometer, we detect the interferogram, that is the contribution of several wavelengths i.e. we measure every wavelength/channel of the spectrum simultaneously. In single channel dispersive experiment however, we always measure the intensity of one wavelength component at a time. This means that to acquire the same spectrum, it takes the FT spectrometer much less time if compared to the dispersive method and for a given measurement time the FT-spectrometer can average a lot of spectra resulting in an improved SNR.

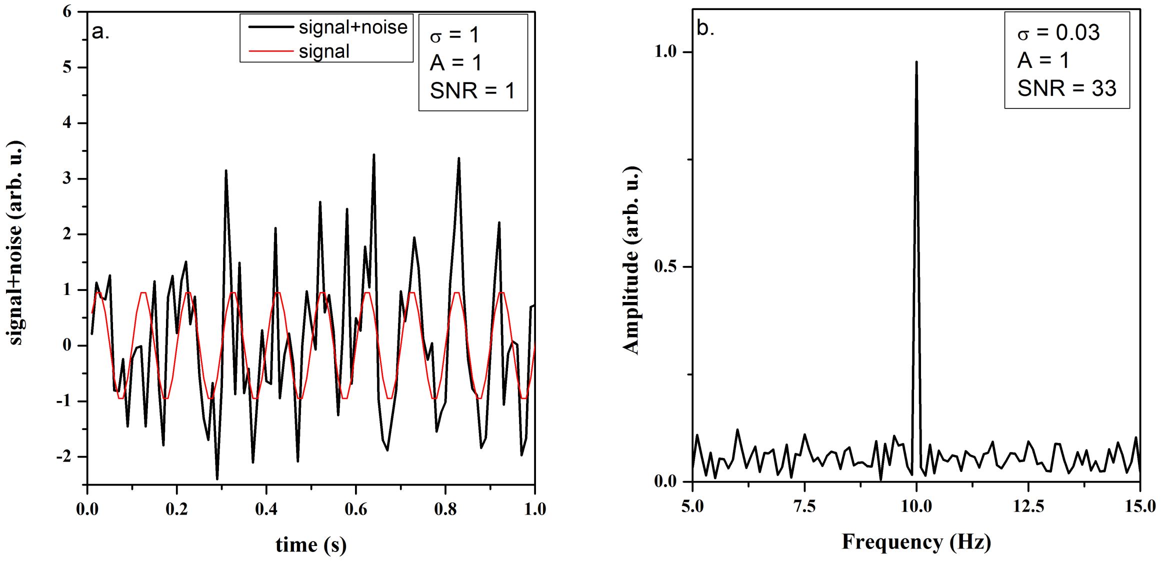

Figure 17: Demonstration of the Fellgett or multiplex advantage. Fig. a. shows a sinusoidal signal (guide for the eyes:red) sampled in $N = 1000$ points, buried in large noise so that SNR = 1. Fig. b. shows the Fast Fourier Transform of Fig. a. : The SNR is dramatically improved, lifting the signal from the noise. The improved SNR here is $\sqrt{N} = 33$

The Fellgett advantage, sometimes called *Multiplex* advantage, is not exclusive to the optical FT-spectroscopy but rather a very general phenomena occurring whenever a signal is measured in the frequency domain and not the time domain. Technically this means detecting in the time domain and applying an FFT algorithm. This property helped to revolutionize the Nuclear Magnetic Resonance or NMR Spectroscopy, and also it can be traced in the metrology of microwave circuits.

The Fellgett advantage states the following: suppose we measure a time dependent signal (e.g. interferogram) in N points. If we apply an FFT algorithm the SNR in the frequency domain will be $\sqrt{N}$ times enhanced compared to the original value in the time domain Eq.(16). This is demonstrated in Fig.17, where σ is the standard deviation of the noise, and A is the amplitude of the signal.

$$\mathrm{SNR}_\omega = \sqrt{N} \cdot \mathrm{SNR}_t \tag{16}$$

Eq.(16) is always true, as the FFT algorithm is only a mathematical operation. However, the noise floor itself (in the time domain) can vary between the FT and the dispersive techniques. The Fellgett advantage in FT-spectroscopy is only true if the noise limit is given by the thermal noise of the photo detector. There are some cases where the noise limit is determined by the noise contribution of the detected signal itself and as the FT technique measures all the photons simultaneously, it will have a greater noise floor in the time domain than the dispersive technique has, i.e. what we gain from Fourier transforming the signal, we lose it on the increased noise in the time domain. Such an example is the shot-noise limited case, where the Fellgett advantage equals 1 [25]. Another noise contribution coming from the signal itself is the oscillator noise (also called flicker noise) with $1/f$ frequency characteristic. In this case the Fellgett advantage of $\sqrt{N}$ turn to a Fellgett *disadvntage* of $\sqrt{N}$. Here the FT technique will have an SNR $\sqrt{N}$ times worse than that of a dispersive one [26]. A general discussion of the various noise sources and their effect on the optical spectrum will be done Sec.2.5.

Connes advantage

In dispersive-spectroscopy, the measured optical spectrum must be calibrated with a sample having known spectral lines e.g. a calibration lamp. Furthermore, the complicated mechanical solutions that governs the mirrors, slits, and gratings present an inherent wavelength instability from spectrum to spectrum. This means that for high accuracy measurment, calibration is not enough after averaging the measured spectra but each spectrum to be averaged must be calibrated. These problems are not present in case of FT-spectroscopy, where each measurement is calibrated by the reference He-Ne laser itself (see the sampling mechanism in the previous section), and as the He-Ne is a gas laser, the wavelength accuracy is very high. This assures a superior wavelength stability of the optical spectra measured with an FT-spectrometer.

2.5 Noise in optical spectroscopy

Understanding the various noise sources in optical spectroscopy is the key for successful instrument development, especially for weak signal measurement techniques as in ODMR. In the following I discuss the main noise sources in optical spectroscopy and their effect on the SNR in the time- and frequency domain.

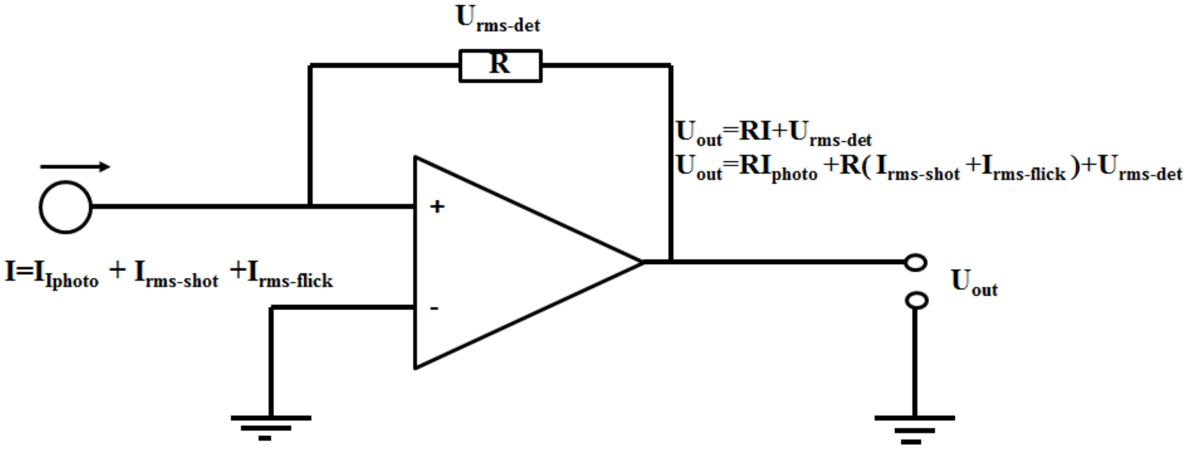

Figure 18: Schematics of the main noise sources of the detected light.

All photo-detectors can be modeled with the electronics shown in Fig.18. The photo diode detects light on the principle of the photoelectric effect, thus it can be modeled as current source. The detected photo-current is amplified with preamplifier, which also serves as a I/U converter, where the amplification is determined by the resistor. In this setup Fig.18 there are three distinct noise sources: detector noise, shot noise and, flicker noise.

The so-called detector noise (thermal noise also Johnson noise) is the noise contribution of the preamplifier and manifests as a voltage noise at the detector's output [27] [28]. The main characteristic is that the measured voltage noise U_{rms} is independent of both the frequency and the detected power of the light Fig20. An important quantity to describe the noise in the frequency domain is the power spectral density $P_{noise}(f)$. It is defined as the noise power U_{rms}^2/R for a 1Hz wide window around a frequency f. The measured noise power is then the integral of the noise power density from DC to the measurement bandwidth Δf. In the case of thermal noise, both U_{rms} and $P_{noise}(f)$ are described by Eq.(17).

$$\begin{aligned} U_{rms} &= \sqrt{4k_BTR\Delta f} \\ P_{noise}(f) &= 4k_BT \\ U_{rms} &= \sqrt{R\int_{f_0}^{\Delta f} P_{noise}(f)df} \end{aligned} \tag{17}$$

The shot noise is the statistical fluctuation of the detected light power. It arises due to the fact that the energy transmitted by the light occurs in a quantized manner

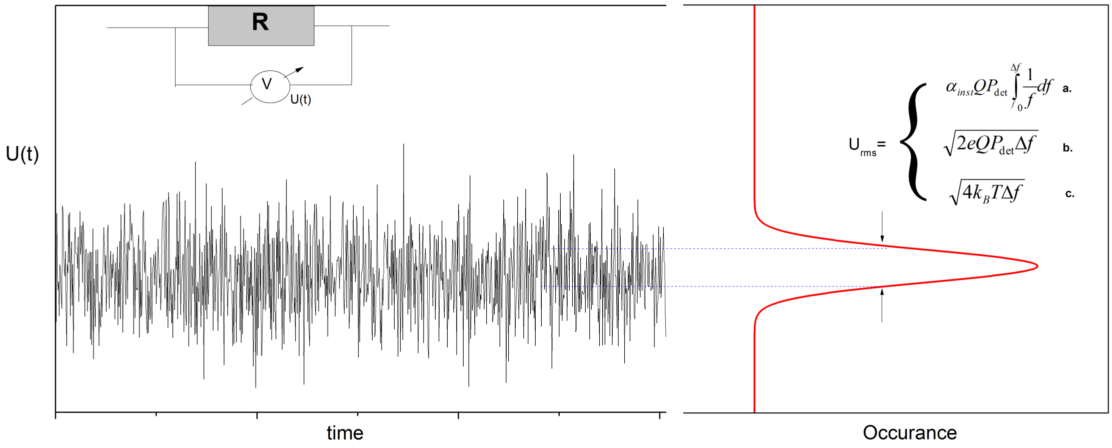

Figure 19: Various noise sources in optical spectroscopy. The noise is defined as the FWHM (U_rms) of the histogram (red curve) of the measured noise floor. Right: the U_rms for a: flicker niose. b: shot noise. c:detector or thermal noise. The meaning of the quantities is described in the text.

($h\omega$ quantums). The photon emission rate of a light source is modeled with Poisson statistics, thus for a process that have $\langle N \rangle$ photon / s expectation value, the variance is $\langle (\Delta N) \rangle^2 = N$ thus the process noise is $\sqrt{N}$. This inherently "noisy" detected light power P_{det} is converted to a photo-current, which in turn will be converted to current noise $I_{rms} = \sqrt{2eI_{det}\Delta f}$ Ref.[shot noise], where e is the elementary charge and I_{det} is the detected photo-current. The ability of the photo diode to convert photons to electrons i.e. P_{det} to I_{det} is described by the *Responsivity* of the detector denoted Q and has the dimensions A/W. The shot noise is also a *white* noise, however, the amplitude of the noise goes with $\sqrt{N} \propto \sqrt{I_{det}} = \sqrt{QP_{det}}$ see Fig.20. thus the value of the detected voltage noise and it's power spectral density are:

$$\begin{aligned} U_{rms} = RI_{rms} = R\sqrt{2eQP_{det}\Delta f} \\ P_{noise}(f) = R2eQP_{det} \end{aligned} \tag{18}$$

The flicker noise (or oscillator noise) is related to the stability of the excitation: if the excitation is unstable in time, than so will be the the photon emission of the sample. This fluctuation of the emission rate around its mean value is detected as a noise, and can be regarded as a current noise from the photo-diode Fig.18. Contrary to the previous two types of noise, here $P_{det}(f)$ is not constant but rather goes with $1/f$, this is referred as *Pink* noise in the literature [29]. The detected flicker noise depends linearly on the detected light power P_{det}, thus the current noise will be $I_{rms} \propto QP_{det} \int_{f_0}^{\Delta f} 1/f df$ Fig.20. The exact value of I_{rms} i.e. the proportionality constant depends on the quality of the excitation laser, and can not be calculated in generaly but rather specific to each construction. Here it is denoted by α_{inst}.

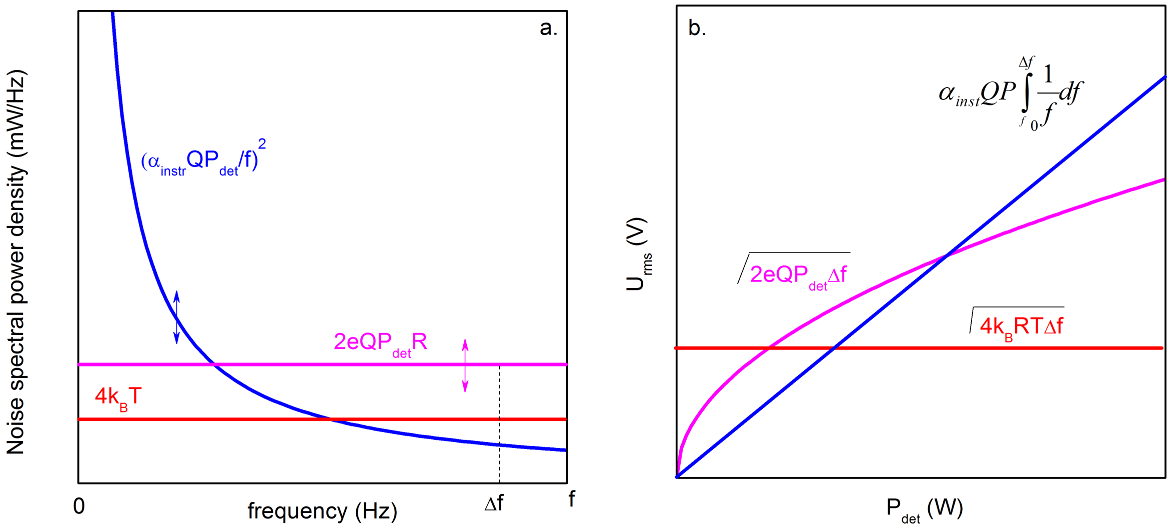

Figure 20: a)shows the frequency dependence of the power spectral density of the 3 main noise sources, along with their values. The red curve is that of the detector noise, the purple is the shot noise and the blue is the flicker noise. Vertical arrows on the shot- and flicker noise curves indicates, that the exact value depends on P_{det}. I show in fig. b. the measured voltage noise as function of light power P_{det}. The value of the noise at a given power is the integral (untill Δf) of the curve inf Fig. a.

The SNR

Generally in an optical spectroscopy measurement all of the three up-mentioned noise sources are present, and the total noise σ_{tot} goes as:

$$\begin{aligned} \sigma_{rms} &= \sqrt{\sigma_{det}^2+\sigma_{shot}^2+\sigma_{flick}^2} \\ U_{rms} &= \sqrt{(4k_BTR+2R^2eQP_{det})\Delta f+(\alpha_{int}P_{det}\int_{f_0}^{\Delta f}\frac{1}{f}df)^2} \end{aligned} \tag{19}$$

Here we assumed that all noise source an uncorrelated therefore they squares of the standard deviations add up. Depending on the P_{det} one of these three term will dominate the noise. For low P_{det} value the noise will be dominated by σ_{det}, as both σ_{shot} and σ_{flick} assumes a small value near zero see Fig.20. This is called *detector noise limit.* By increasing P_{det} (i.e. increasing the excitation power) the shot noise will increase with $\propto \sqrt{P_{det}}$, and for intermediate P_{det} values will be the dominant noise:*Shot noise limit.* Further increasing P_{det} will eventually let the flicker noise be the dominant noise source: *flicker noise limit.* In case of detector noise limit, the SNR will increase linearly with the excitation power as the signal do so and the noise is independent of P_{det}. In the shot noise limit, the SNR will only increase by the square root of the excitation power. Finally when the flicker noise limit sets in the SNR will not increase anymore, as both the signal and the noise are linear in the excitation power. This is depicted in Fig.21.

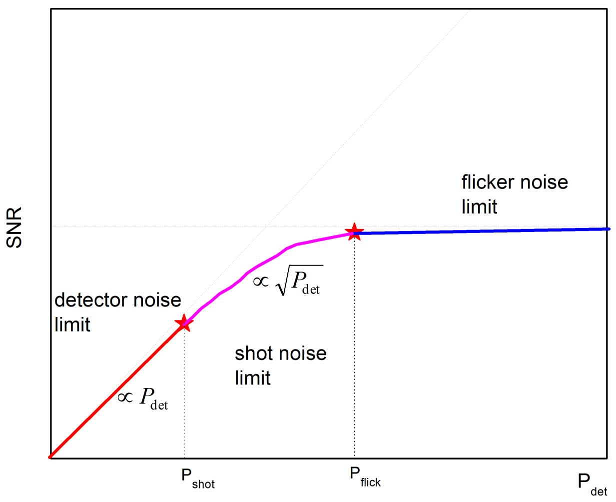

Figure 21: The dependence of the spectrum SNR on the detected light power P_{det}. P_{shot} indicates the amount of detected power where the shot noise starts to dominate. There the SNR increment will turn from linear to $\sqrt{P_{det}}$. P_{flick} indicates the power level where flicker noise limit sets in. From there the SNR will set to a constant value.

3 Experimental developments

3.1 An FT-Raman spectrometer with visible excitation

This section discusses a development which was published in Ref.[10]. The main reason of the popularity of the FT-spectrometers is the Fellgett advantage (see Sec.2.4.3). However, in our case there is an important difference between the multiplex advantage, and the Fellgett advantage. The multiplex advantage is an inherent property of the FT method and it describes the decrease of the noise when going from the time domain to the frequency domain (FFT) Eq.(16). On the other hand, the Fellgett advantage is the ratio between the FT method SNR (SNR_{FT}) and the dispersive, single channel spectrometer $\mathrm{SNR}_{disp.-sch}$. The Fellgett advantage is also true for dispersive spectrometer with CCD detector (multichannel).

$$F = \frac{\mathrm{SNR}_{FT}}{\mathrm{SNR}_{disp.-sch}} \tag{20}$$

The main difference is that the Multiplex advantage is always $\sqrt{N}$, where N is the number of the measurement points of the interferogram, while the value of the Fellgett advantage depends on the nature of the noise i.e. it is not fixed. In case of the detector noise limit, $F = \sqrt{N}$ but in the case of shot noise limit $F = 1$. The latter is due to the fact, that the FT method is a multichannel method, and it measures all the photons simultaneously i.e. the noise contribution of the FT method is proportional to the square root of the integrated power of the spectrum Eq.(18), whereas in the case of the disp.-sch method, the shot noise is given by the photons of only the measured wavelength, thus the noise itself in the time domain is not equal.

To better understand the degradation of the Fellgett advantage in the shot noise limit, let us consider the following example: suppose a boxcar spectrum (for simplicity) from 0 to k_{max} wave number is resolved in N points in a dispersive single channel spectrometer. If the integrated intensity is M cps, then the average detected intensity is M/N cps Fig.22(a). As the intensity in one channel is M/N, than the shot noise will be $\sqrt{M/N}$, thus $\mathrm{SNR}_{disp.-sch} = \sqrt{M/N}$. In the case of an FT-spectrometer, the intensity is still M/N cps, however, the noise will be $\sqrt{M}$, as we are measuring every photon simultaneously, hence the $\mathrm{SNR}_{FT} = \sqrt{M}/N$ in the time domain. After Fourier transformation, this is further enhanced by $\sqrt{N}$ (Multiplex advantage), thus the SNR in the frequency domain will be $\mathrm{SNR}_{FT} = \sqrt{M/N}$ and the Fellgett advantage drops to unity.

The degradation of the Fellgett advantage is a direct consequence of the fact that the measured spectrum is approximated by a constant intensity line, as therein the total photon flux is evenly distributed among all the measured channels. This approximation is good for broad band optical spectra, like Transmission-, Absorption- and even PL spectra. Contrary to this, the Raman spectra are characterized by few, well defined narrow peaks, thus here the boxcar spectrum approximation is not valid. We can model the Raman spectra by an instrument-resolution limited measurement i.e. the spectrum is a very narrow line at only one wavenumber (see Fig.22(b)). In this case the detected intensity M/N cps equals the total photon flux, thus the shot noise will be $\sqrt{M/N}$ in the time

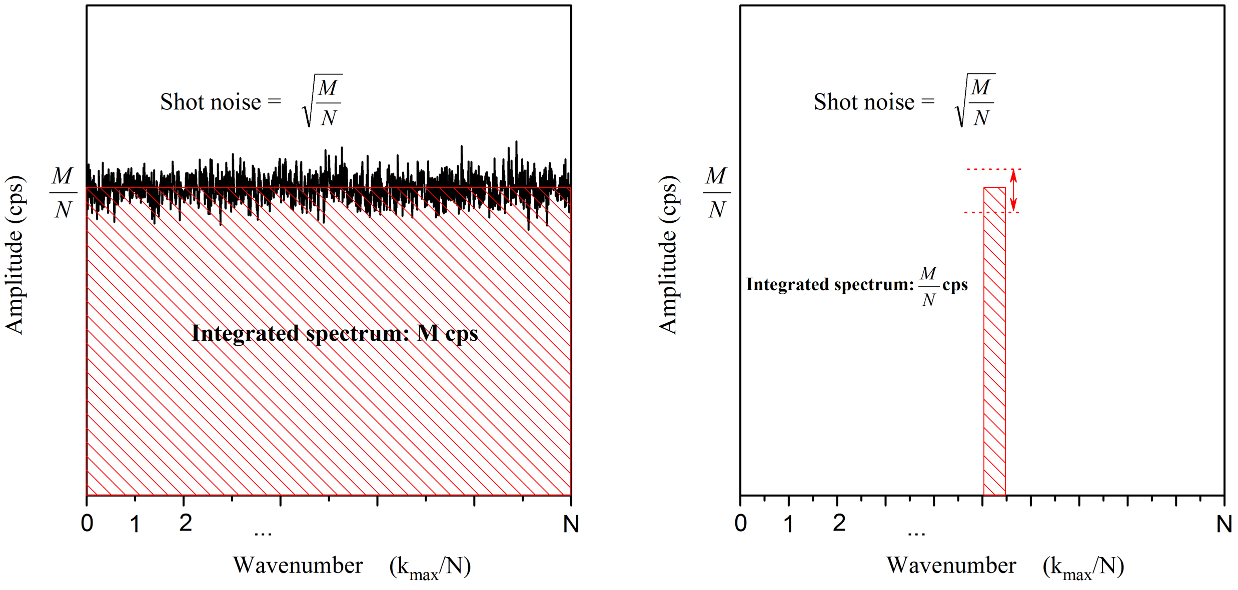

(a) Fig. 1 (b) Fig. 2

Figure 22: a): A boxcar spectrum of k_{max} optical BW and a total photon number of M resolved in N points by a disp.-sch spectrometer. The shot noise is $\sqrt{M/N}$. In case of FT the shot noise is $\sqrt{M}$, thus the Fellgett advantage drops to unity. b): A single line, narrow spectrum, where the resolution is limited by the instrument. Arrow denotes the shot noise. Here, the shot noise is equal for both FT and disp.-sch methods, and the Fellgett advantage is again $\sqrt{N}$.

domain for both FT and disp.-sch methods, and again the Fellgett advantage will be $F = \sqrt{N}$ even in the shot noise limit. This suggests, that contrary to the common sense, VIS-FT Raman spectrometer does not suffer substantially from SNR degradation due to the shot noise.

The recent advances in the industry of photo-detectors made the CCD devices commercially available. Nowdays -in dispersive spectrometers- the PMT detectors are displaced by truly multichannel CCD detectors, where every wavelength of the spectrum is simultaneously measured. This enhances the SNR of the disp.-sch by a factor of $\sqrt{N}$ (providing that the pixel number of the CCD is enough to cover the whole spectrum of interest). Again the SNR$_{FT}$ is degraded to $F = 1/\sqrt{N}$ (Fellgett disadvantage) and $F = 1$ respectively for broad band and narrow band optical spectra.

The Fellgett advantage of the FT method compared to disp.-sch and disp.-CCD methods in case of broad band and single peak narrow band spectra are presented in Table.2. Finally, we also define the Fellgett advantage in case of CCD based dispersive spectrometers, which always equals the pixel number of the CCD, regardless of the noise type: $F = \text{SNR}_{disp.-CCD}/\text{SNR}_{disp.-sch} = \sqrt{N_{pix}}$.

Spectrum	Reference method	F
Broad	disp.-sch	1
Single peak	disp.-sch	$\sqrt{N}$
Broad	disp.-CCD	$1/\sqrt{N}$
Single peak	disp.-CCD	1

Table 2: The Fellgett advantage for various types pf spectrometers

3.1.1 The spectrometer setup

Following the overall principles in instrumentation, the setup was motivated to maximize the signal and minimize the noise of our spectrometer. The earlier is achieved by using i) an aberration free, high-speed (i.e. small $f/\#$) light-collection objective and ii) optical elements (mirrors and beamsplitter) and detector which is optimized for visible light. Since shot-noise limits the performance of our spectrometer, unwanted light sources has to be eliminated. This is achieved by using three high performance interference filters, a pinhole, and a darkened environment.

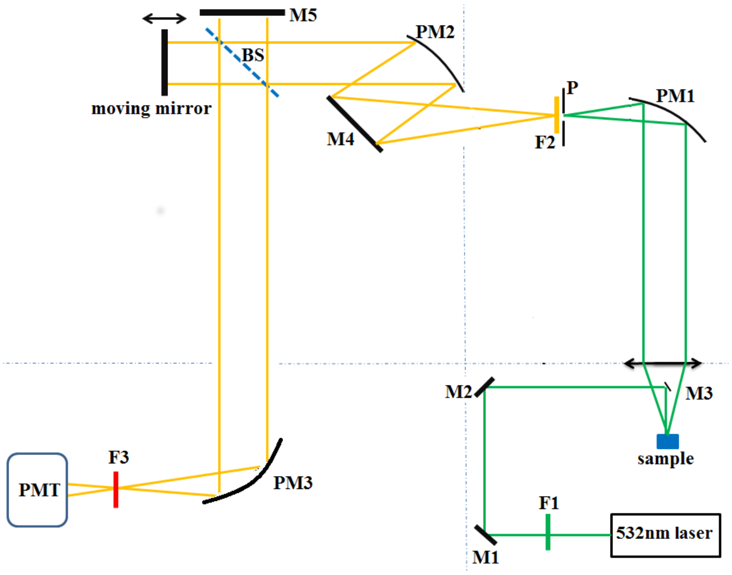

Figure 23: Schematics of the visible laser based FT-Raman spectrometer.

The spectrometer setup is shown in Fig. 23. It is based on a commercial infrared Fourier-transform (FT-IR) and Fourier-Raman (FT-Raman) spectrometer (*Bruker IFS66v with FRA 106 Raman module*). The FT-Raman spectrometer was optimized for excitation with a 1064 nm Nd:Yag laser, i.e. for the NIR range. Several optical elements including the exciting laser, collecting objective, guiding optics, beamsplitter, and detector were replaced with ones suitable for operation in the visible optical range. The spectrometer is divided into four functional parts: sample compartment, light collecting compartment, the interferometer, and the detector compartment.

A frequency doubled Nd:YAG solid state laser at 532 nm is used (*Optotronics Inc. VA-I-100-532 100 mW*) for excitation with a beam diameter of 1.2 mm. A 650 nm short pass filter, F1 (*Thorlabs FES0650*), removes the 812 nm radiation output from the laser. The laser beam is guided to the sample with two dielectric mirrors (M1 and M2) and a small (3x3 mm) right angle prism M3, (*Edmund Optics #47-921*). This is the usual setup for the so-called macro-Raman configuration, i.e. when the excitation and the scattered Raman light are separated (or duplexed) according to the different beam sizes. We note that the light is not focused on the sample in this configuration. This is possible for FT-Raman spectrometers, where the light does not need to come from a well focused source as there is no input slit in contrast to dispersive spectrometers (Jacquinot advantage Sec.2.4.3).

The light is scattered from the sample in a 180° geometry and is collected with a state-of-the-art, eight element double-Gaussian objective lens (50 mm $f/0.95$, *Navitar DO-5095* of eight optical elements). The objective produces a 1.8" diameter beam which is focused by a 2" 90° off-axis parabolic mirror, PM1 (*Edmund optics, NT63-186, Aluminium coated*) on a pinhole, P, of 2 mm diameter. There is a 1" diameter 532 nm long-pass filter (LPF), F2 (*Semrock LP03-532RE-25* before the pinhole. The LPF has optical density 7 (OD7) rejection for the stop-band and $> 93\,\%$ transmission for the pass-band. The transition edge of the filter can be fine tuned by rotating around a vertical axis [30] as the edge blue shifts when rotated away from normal incidence. The LPF efficiently filters out the undesired quasi-elastic (near 532 nm) radiation, which is commonly referred to as *Rayleigh radiation* and it allows only the Stokes Raman radiation to pass. The light is incident on the interference filter with a maximum angle of $\theta = 8°$ which broadens the $tr = 93\,\mathrm{cm}^{-1}$ transition range of the LPF (where transmission changes between OD6 and OD0) according to Ref. [31]:

$$tr' = tr + \lambda_0 \left(1 - \sqrt{1 - \frac{sin^2\theta}{n^{*2}}}\right), \tag{21}$$

where $n^* \sim 1.5$ is the index of refraction of the filter material and $\lambda_0 = 18797\,\mathrm{cm}^{-1}$. Eq.(21). yields a somewhat larger transition range of $tr' = 133\,\mathrm{cm}^{-1}$ of the LPF, which does not affect its performance. The use of this moderately focused geometry eliminates the need for an LPF with 2" diameter. We found that the order of the LPF and the pinhole is important: light reflected from the front side of the LPF can reflect toward the spectrometer for a reversed order, which deteriorates the performance. We found that the pinhole reduces the intensity level of the Rayleigh light by a factor of 3 without affecting the Raman signal.

The interferometer compartment was unchanged with respect to the commercial setup. Therein the Raman light is collimated and guided to the interferometer with a planar, M4, and a parabolic mirror, PM2. A Michelson-type interferometer produces the interferogram with the standing mirror, M5, a moving mirror, and a quartz beamsplitter, BS (*Bruker T502/1*) optimized for 470-833 nm). We used 5 kHz scanning speed of the interferometer but other values between 500 Hz and 10 kHz are possible with the IFS66. The intensity modulated beam produced by the interferometer enters the detector compartment where it is focused by the parabolic mirror PM3 on a 633 nm short pass filter (SPF), F3 (*Semrock SP01-633RU*), to eliminate the 632.832 nm line of the He-Ne acquisition laser. The optical bandwidth (OBW) of the spectrometer is thus given by the two filters (532 nm LPF and

633 nm SPF) and is $532 - 633\,\mathrm{nm}$. This OBW corresponds to a maximum of $3000\,\mathrm{cm}^{-1}$ Stokes Raman shift with respect to the 532 nm excitation, which is sufficient for most Raman studies. The range could be extended towards longer wavelengths by using a stop-band filter instead of the 633 nm short pass filter. Alternatively, our spectrometer could be readily modified to detect anti-Stokes Raman scattering by replacing the 532 nm long-pass filter by a short pass filter.

A photo multiplier tube, PMT, (*Hamamatsu R955*, 160-900 nm, Q.E.$\approx$ 10%) followed by an I/V converter (*Hamamatsu C7319*) is used to detect the interferogram. The PMT cathode-anode voltage can be set up to 1500 V and the corresponding PMT gain is obtained from its datasheet. The I/V converter can be set for either 20 or 200 kHz bandwidth (BW) and 10^5-10^7 gain. The IFS66 instrument internally sets a BW that is near the scanning speed of the interferometer, which is optimal for this measurement. The latter information was obtained by comparing the noise in the signal digitized by the IFS66 to that obtained using an external analog-to-digital converter. Noise of a PMT is known to be due to shot noise and the signal-to-noise ratio for a given cathode current, I_c, is [Ref. [32]]:

$$S/N(I_\mathrm{c}) = \sqrt{\frac{I_\mathrm{c}}{2e\mathrm{BW}}}, \tag{22}$$

where e is the elementary charge. We note that Eq. (22). is valid irrespective of the origin of the cathode current as it can be due to light or due to dark current (thermal fluctuations or cosmic radiation).

3.1.2 Performance of the spectrometer

The performance of the VIS-FT Raman spectrometer was characterized using powder sulphur sample, as it has strong Raman lines and it is often used as a benchmark sample. In Fig.24 I show the interferogram of sulphur, recorded with 10mW excitation power, 5kHz mirror velocity, $4\mathrm{cm}^{-1}$ resolution and single scan (0.9 s). The interferogram can be converted back to cathode current I_c by knowing the conversion value of the I/V converter and the PMT gain (data sheet).

The average value of the cathode current is $I_c = 11.2\mathrm{pA}$. The noise has a Gaussian distribution with $\sigma = 0.2\mathrm{pA}$, that was calculated from the interferogram part, where the interference pattern has already decayed. The quality of the interferometer is characterized by the so-called *fringe visibility.* In an ideal interferometer the interferogram of a coherent light is a perfect cosine Eq.(5), after which the FFT (the spectrum) shows it's amplitude, thus every photon participates in the interference pattern. In this case we say that the light entering the interferometer is completely modulated, as the amplitude of the interferogram equals that of the baseline. The fringe visibility fv is defined as Eq.(23), where I_{max} and I_{min} are the maximum and minimum of the interferogram respectively Fig.24.

$$fv = \frac{I_\mathrm{max} - I_\mathrm{min}}{I_\mathrm{max} + I_\mathrm{min}} \tag{23}$$

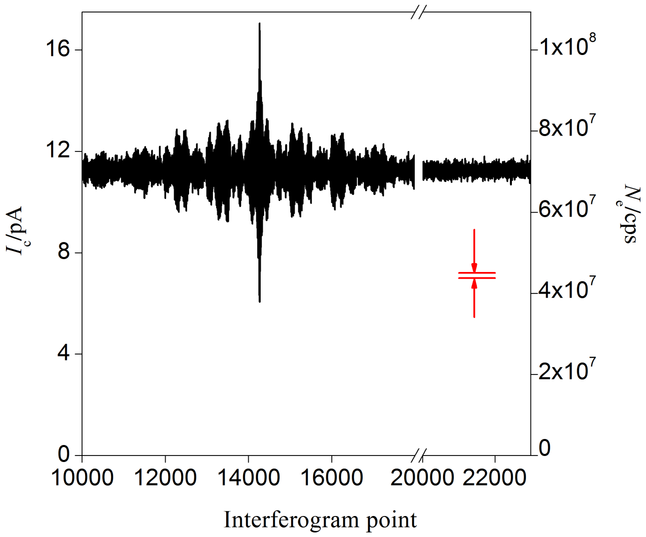

Figure 24: Interferogram of sulfur powder given in units of the photomultiplier cathode current. The corresponding number of cathode electrons is also given. The noise ($\sigma = 0.2pA$) of the current is obtained from the part of the interferogram where the coherent light has decayed and its magnitude is shown between arrows (offset for clarity). The fringe visibility is about 0.5, indicating the presence of unmodulated light on the detector

For an ideal interferometer the $fv = 1$. However for a real interferometer $fv < 1$ for the following reasons:

1. The interferometer is misaligned and there are some rays that travel more than the coherence length, thus they do not interfere.
2. The entering light is not well collimated. Again there are some rays that travel more than the coherence length.

This directly effects the SNR of the spectrum as the signal itself is proportional to the $I_{max} - I_{min}$ (sensitive on the alignment), whereas the noise is usually proportional to $\sqrt{I_{max} + I_{min}}$ in the shot noise limit. The fringe visibility in our case is $fv = 0.5$, which is typical for VIS-FT interferometer [33], i.e. half of the light entering the interferometer is unmodulated and does not contribute to the signal (but does so to the noise). As discussed in Eq.(22), the SNR is defined by the cathode current. For $I_\mathrm{c} = 11.2$pA this would yield an SNR = 86, which is in a good agreement of the SNR = 56 obtained experimentally Fig.24, which proves, that we are operating in the shot noise regime.

The Raman spectrum of the sulphur Fig.25 was obtained from the interferogram in Fig.24. The characteristic Raman lines of sulphur at 86, 147, 188, 215, 247, 434, and 472 cm^{-1} are easily recognized. Additional peaks due to the He-Ne acquisition laser and the Rayleigh scattering are observed, however they are significantly weaker than the Raman lines. If these, otherwise strong additional lines are not suppressed enough, they would largely contribute to the noise (as the measurement is shot noise limited), or completely saturate the photo-detector. The integrated SNR (integrated signal / noise) gives $\mathrm{SNR}_{integrated} = 6350$ this should be compared to the $\mathrm{SNR}_{interferogram} = 56$ in the time

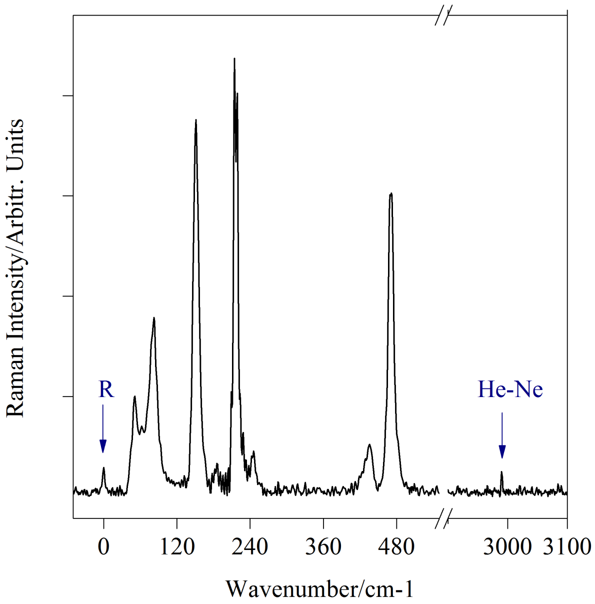

Figure 25: Sulphur Raman spectrum measured with VIS-FT spectrometer. Additional peaks to the Raman lines appears due to the He-Ne acquisition laser and the Rayleigh scatterin (R)

domain, as there the baseline value also corresponds to the total number of photons. The obtained experimental multiplex advantage is 113. Considering that the interferogram in Fig.24 was sampled in $N = 15800$ points, the experimental multiplex of 113 agrees perfectly with the calculated$\sqrt{15800} = 125$ Eq.(16). To meaningfully compare the performance of the VIS-FT spectrometer to the dispersive technique, I define the SNR as the ratio of the largest Raman peak at $218 cm^{-1}$ to the noise taken from 750-1500 cm^{-1}. Note that this is not the same as the integrated SNR defined previously. For our construction the SNR yields SNR = 156 when normalized to 1 second measurement time.

3.1.3 Comparison to dispersive spectrometers

The SNR performance of the VIS-FT spectrometer was compared to two dispersive spectrometers: A home built single channel and a CCD based multichannel one. The earlier was based on a 320 mm spectrograph equipped with a 2400 grooves/mm grating *Jobin Yvon iHR320*, and the same f/0.95 objective and laser that was used for the visible FT-Raman spectrometer. The latter was a state-of-the-art commercial Raman spectrometer *Horiba Jobin-Yvon: LabRAM-HR800* [30] equipped with a 532 nm laser and a 1024 pixel CCD photo-detector *Horiba Symphony II* a 600 grooves/mm grating and 800 mm focal length. The collecting objective was a microscope *Olympus LMPlan 50x/0.50, inf./0/NN26.5* with N.A.=0.5 that yields about $1.3x1.3 \mu m^2$ spot size. For a valid comparison, the same sample was measured with the same acquisition parameters (spectral window, laser power, resolution) as in case of the VIS-FT spectrometer.

The spectra in Fig.26 suggest that the noise of the VIS-FT measurement is greater to that of the dispersive techniques. Due to the multiplex effect of the Fourier transformation, the noise of the interferogram is evenly distributed in the frequency domain, thus the base

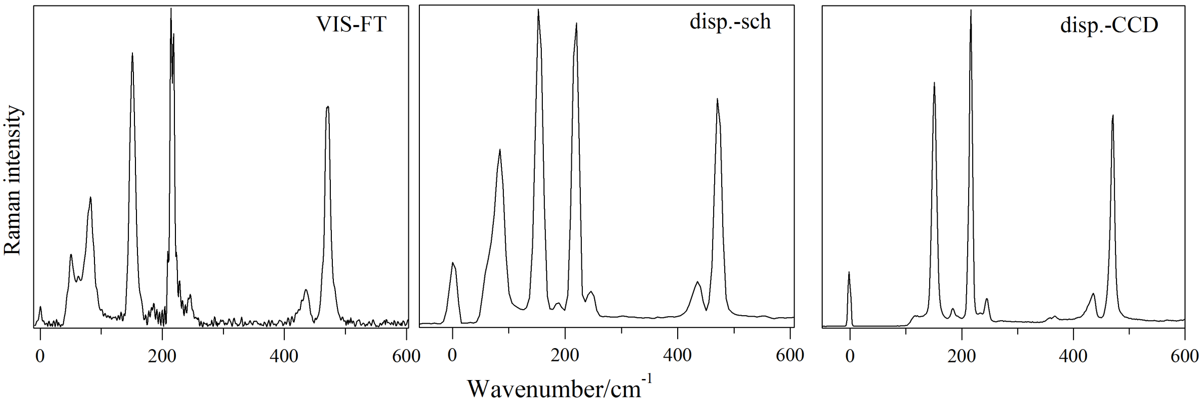

Figure 26: Sulphur Raman spectrum measured with three different spectroscopic techniques: FT, dispersive single channel and dispersive multichannel (CCD detector). Seemingly the FT method has worse SNR than the other two techniques. However, in case of the dispersive methods, the shot noise is located on the peak, whereas the baseline is detector noise limited. Note that due to the different LPF edge position, the spectra are not identical between 0 and $100cm^{-1}$.

line is shot noise limited. However, this is not the case with the dispersive methods, as there the shot noise is located on the peaks, i.e. the base line is detector noise limited, which is considerably less than the shot noise.

We find that the noise value of the VIS-FT technique is well defined, where as in the case of the dispersive methods it is wavelength dependent, thus the question arises: What should we consider as noise value in case of the dispersive method? To answer this question, we should remember the main task of optical spectroscopy: determining the line parameter in the spectrum such as the line position, width, amplitude etc. Theses quantities are usually determined from fitting the lines. The errors of the fit are primerly determined by the noise, thus it is straightforward to approach the noise of the dispersive technique from this angle of view. I define an *equivalent uniform noise* for the dispersive measurements, that yields the same errors for the line fitting as the wavelength dependent noise does Fig.27. I found that an effective noise amplitude of $\sigma = \sqrt{S/L}$ (S: signal amplitude, L: signal FWHM) describes the shot noise effect satisfyingly, thus the total noise σ_t Eq.(24), where σ_D is the dark-current noise (detector noise).

$$\sigma_{\mathrm{t}} = \sqrt{\sigma_{\mathrm{D}}^2 + \frac{S}{L}} \tag{24}$$

For sulphur a typical $S \approx 10000cps$ and $L \approx 10pixels$ is observed in case of the disp.-CCD measurement. Thus we obtain a total noise of $\sigma_t \approx 30$ which is a factor of 10 larger then the detector noise floor, taken from the baseline. I calculate the SNR for the three spectrometers(single-channel, CCD-based, and FT) from the measurements Fig.26 with these considerations and normalized it by the same measurement time. I obtain $\mathrm{SNR}_{disp.-sch} = 19$, $\mathrm{SNR}_{disp.-CCD} = 815$, and $\mathrm{SNR}_{FT} = 156$ for the single-channel, CCD-based dispersive and FT spectrometers respectively. The corresponding Fellgett

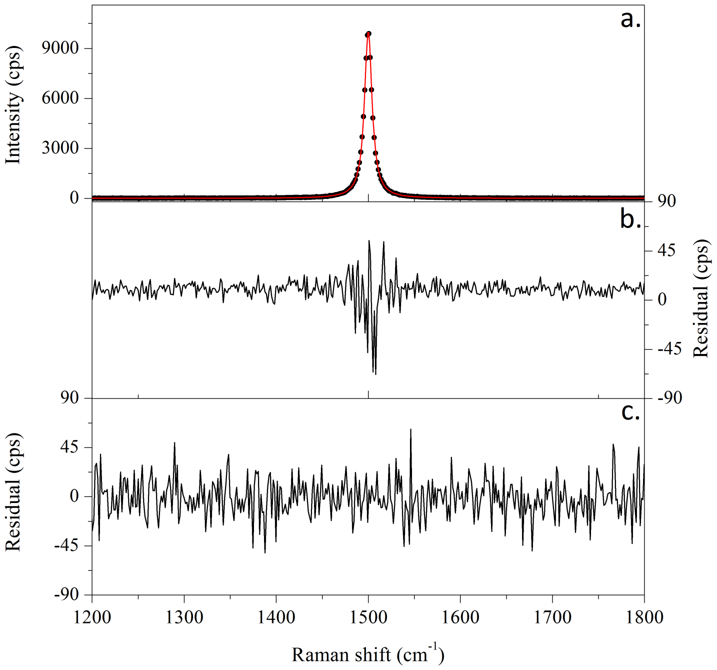

Figure 27: a): simulated shot noise for CCD superimposed on a Lorentzian lineshape, along with the fit. Fig. b. shows the residual of the fit. The noise is located on the peak. I found that an equivalent uniform noise, with the value of $\sqrt{\text{Amplitude}/linewidth}$ effectively describes the shot noise in Fig. c.

advantages are $F = 43$ for disp.-CCD and $F = 8$ for VIS-FT.

We find that in accordance with Table.2, we have a Fellgett advantage when compared to the disp.-sch

3.1.4 Discussion of the Raman spectrometer design

The Fellgett advantage

At the beginning of this section, I argue that the FT method still holds the Fellgett advantage even in the shot noise limit, when the spectrum is not broadband. This was proved in the instrument-resolution limited single peak case Fig.22(b). This is somewhat oversimplified picture, as in reality, the spectrum contains several resolved lines with finite width. A more general approach should be developed, that accounts for the number- $P_\sharp$ and the width L of the peaks. In case of comparison with disp.-CCD, we should consider technical parameter such as the CCD's pixel number N_{pix} , the Quantum Efficiency (QE) and finally the fact that the total measurement points of the whole spectrum is usually more than N_{pix}, i.e. the spectrum is only covered with several measurements, whose number is denoted by G.

	Fellgett advantage	reference single channel method
FT-Raman/NIR	$\sqrt{N_{\rm ch}}$	disp.-sch/NIR
disp.-CCD/VIS	$\sqrt{5\,N_{\rm pix}/G}$	disp.-sch/VIS
FT-Raman/VIS		
single peak	$\sqrt{N_{\rm ch}}$	disp.-sch/VIS
broadband	1	
Raman-like	$\sqrt{\frac{N_{\rm ch}}{P_\sharp L}}$	

Table 3: The Fellgett advantage factor for the different techniques with respect to the corresponding single-channel detection method. We give values for three separate cases (single peak, broadband, and Raman-like spectra) for the FT-Raman/VIS spectrometer. The symbols, $N_{\rm pix}$, $N_{\rm ch}$, G, $P_\sharp$, L and the spectrometer types are defined in the text.

Table.3 summarizes the Fellgett advantage of the disp.-CCD and FT techniques relative to the disp.-sch method for the VIS regime (shot noise limit) and the NIR regime (detector noise limit). In the NIR regime I had already discussed that the $F = \sqrt{N_{ch}}$. In the visible regime the disp.-CCD would be $F = \sqrt{N_{pix}}$, however the QE ($\approx 50 - 70\%$) of a CCD is typically 5 times greater than the PMT's QE ($\approx 10 - 15\%$). In the shot noise limit, increasing the signal with a factor of 5 increases the SNR with a factor of $\sqrt{5}$. This is also modified by the number of measurements G, that it take the CCD to cover the spectrum. In case of VIS-FT, the Fellgett advantage is $\sqrt{N_{ch}}$ for a single unresolved peak and 1 for a broadband peak, as already discussed. For a Raman spectrum consisting of $P_\sharp$ lines of equal amplitude and each having w spectral line-width, which is L times larger than the spectral resolution, we obtain $\sqrt{\frac{N_{ch}}{P_\sharp L}}$ for the multiplex advantage. This formula recovers the extremal cases of the single peak ($P = 1$ and $L = 1$) and the broadband spectrum ($P = 1$ and $L = N_{ch}$). In case of our measurement, the parameters for LabRam yields $\sqrt{5\,N_{\rm pix}/G} \approx 50$ and VIS-FT $\sqrt{\frac{N_{ch}}{P_\sharp L}} \approx 14$. These values are to be compared with 48 and 8 respectively, thus the calculated and measured multiplex advantage values are in good agreement for both kinds of spectrometers.

The throughput advantage

Most of the modern Raman spectrometers that operate in the visible regime utilize CCD detectors and are coupled to a microscope (Micro-Raman setup) i.e. they posses the Fellgett advantage and do not suffer from low throughput (Jacquinot advantage). We see that in Raman spectroscopy the VIS-FT principle shows similar performance as state-of-the-art multichannel dispersive spectrometers, when the Fellgett advantage is considered. What makes the FT method really competitive to the CCD based dispersive is the different nature of the Jacquinot advantage in the case of the two setups: In multichannel dispersive method the Jacquinot advantage is achieved on the expense of increasing the laser power density on the sample (Diffraction limited spotsize). This imposes a limit on the power of laser exciting the sample, typically $\approx 1\,\mathrm{mW}$. On the contrary FT spectrometer inherently possesses the Jacquinot advantage. Moderate (or non at all) focusing is only required to avoid degradation of the resolution Table.1. The maximum diameter of the spot size can be calculated Eq.(13). In this case using $f = 50\,\mathrm{mm}$,$\delta k = 4cm^{-1}$ and $k_{\max} = 18796$ (532 nm)results a laser spotsize of 1.45mm which is larger than in our VIS-FT (1.2 mm), thus no focusing at all is required. The Damage threshold power scales with $(\frac{d_{FT}}{d_{micro}})^2$, where d denotes the laser spot diameter for the FT and Micro-Raman setup respectively. Thus the damage-threshold for VIS-FT is 10^6 times higher than that of the dispersive micro setup. The real manifestation of the Jacquinot advantage in our case, is this immense room to increase the exciting laser power on the sample, i.e. the SNR of the Micro-Raman setup is limited, whereas in case of VIS-FT basically no such limit exists.

3.2 Development of a Fourier-transform PL spectrometer

In this section I present the development of a Fourier principle based PL spectrometer. The setup is uniquely designed to suit PL measurements of SWCNTs. Although it is not reported herein, this development constitutes the first step toward an FT based ODMR spectrometer which is to be developed later.
Contrary to common PL spectrometers where a broadband lamp is used as excitation, here we use a tunable laser. This way much higher excitation energy-density can be achieved than most of the commercial setups. Also the tunable laser is required to address CNTs only with specific chirality. This is achieved when the excitation energy matches that of a resonant optical transition (which in turn is uniquely determined by the chirality vector) Fig.3. The developed FT-PL spectrometer is coupled to an existing measurement setup, that utilize a dispersive single channel spectrometer *Jobin-Yvon iHR 320*, that was used for comparison in case of VIS-FT Raman. At the end of this section I also discuss how the sensitivity of this existing dispersive based PL setup be further increased using the Ge detector of the FT-PL setup.

3.2.1 The Spectrometer setup

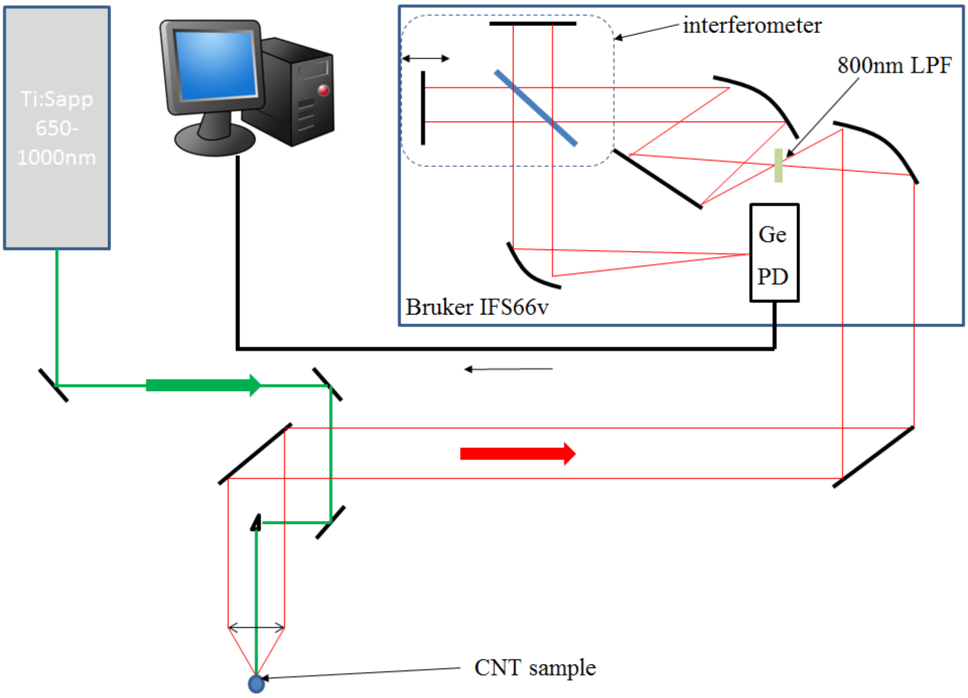

Figure 28: The schematic representation of the FT-PL setup. The PL light of the CNT sample is coupled to the Bruker spectrometer by a periscope system (red line/arrow).

The excitation and light collection

We use a Nd:YAG (532 nm 5W) pumped Ti:Sapp tunable laser for excitation. Its lines can be tuned from 700 nm to 1000 nm and it is used at an average 670 mW output

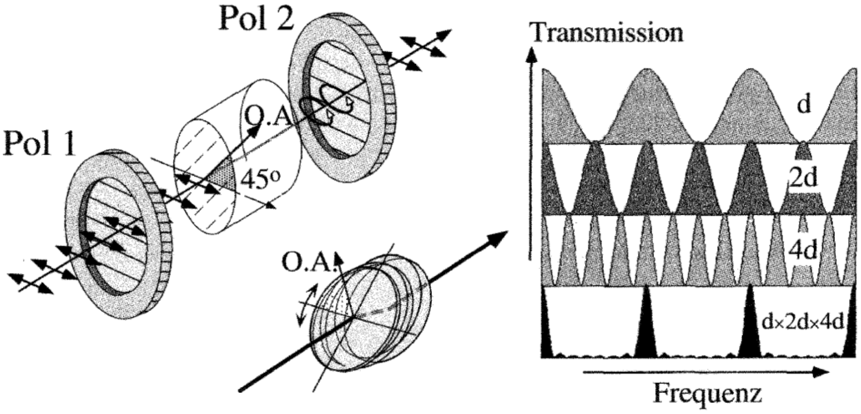

Figure 29: Schematic layout of a Liot filter and the wavelength transmission function. Figure from Ref.[35].

power. The beam is externally attenuated to 1-100 mW with a pinhole. The wavelength selection is realized by using a *Lyot filter* [34]. It is a series of (ever thickening) beriferingent (Quartz) crystals placed between two polarizers, where both polarization axis are parallel. Suppose the incoming light is horizontally polarized, then it will pass the first polarizer plate. A beriferingent crystal with length d whose Optical Axis (OA) is set at 45° with respect to the horizontal direction as shown in Fig.29 will rotate the polarization plane. This is because the speed of light for the two circularly polarized light differ (beriferingence effect). An incoming horizontally polarized light is a superposition of two opposite circularly polarized components with 0° phase shift, thus when propagating in the beriferingent crystal, a phase shift between the two circular components will be introduced at the end of the crystal (due to the different speed of light). This phase shift in turn, will rotate the polarization plane out of the originally horizontal, thus when hitting the second polarizer, the intensity of the light will be decreased. Obviously the introduced phase shift (and with it the polarization rotation) is wavelength dependent. If the thickness d is set such, that it acts as $\lambda/2$ plate for a certain λ wavelength, then there will be no transmitted light. The transmission for the same d thick plate will be one for a wavelengths $(n + \frac{1}{2})\,\lambda$, as for them the phase shift will be $n \cdot 360°$, thus the wavelength dependent transmission has a cosine periodicity with a period separation of λ. If the crystal plate is chosen to be $2d$ thick, then this periodicity doubles and for $4d$ it will again double. Now if these crystals are placed behind each other than the total transmission is the multiplication of the three separate transmissions see Fig.29, thus we have a very narrow wavelength selection. By rotating the degree of the OA with respect to the horizon, we can adjust the extincition condition for different wavelengths i.e. by rotating the Quartz crystals we can move the peak of the transmission curve for higher (or lower) wavelengths.

For the scattered light collection, we use the so-called 180° geometry: the laser beam is directed to the sample by a small 3 mm prism and focused with a 1 inch aspheric doublet *lens* $(f/\sharp = 1)$ that also collects the scattered photons from the sample. The prism serves as a duplexer: it directs the $3mm$ wide beam to the sample, but the the scattered light (2.53 cm wide collimated beam) passes through it, and is further coupled to the FT-IR spectrometer by a periscope system Fig.28.

The spectrometer

I use the same IFS66v Bruker FT-IR spectrometer used for the VIS-FT Raman to be able to record the PL spectrum of CNTs. The schematic layout of the optical path is depicted in Fig.28. Neither the excitation nor the sample compartment are part of the spectrometer. The scattered light is coupled to the FT-IR spectroemter with a periscope system Fig.28. I use a 800 nm *Thorlabs* LPF to get rid of the elastically scattered light (Rayleigh scattering), due to the same reasons discussed in the VIS-FT Raman construction.

	AC_{pkpk}	DC	fv
Bruker-RT objective	1.2 V	1.416 V	0.43
Bruker-Cryo objective	200 mV	253 mv	0.4
Navitar 2 inch	144 mV	215 mV	0.34
measured at 1.6 kHz			

Table 4: Value of fv depending on the employed objective. Values are corrected with the detector's cut-off effect @ 1.6 kHz mirror velocity.

To assess the quality of the interferometer, I measured the fv with three different objectives, designed for operation in the NIR band. I used the Raman spectrum/interferogram of Sulphur (but now in the NIR regime) to acquire the fv. fv was evaluated as the ratio of the peak to peak value AC_{pkpk} and the $2 \cdot DC$ offset in the interferogram, measured with an oscilloscope. I have found that the value of fv is sensitive on the objective I use, i.e. how well is the laser spot focused and the collected light is collimated. The typical values for PL measurements range between $fv = 0.35 - 0.4$ Table.4. Thus we lose approximately a factor 3 in the SNR due to the limited fringe visibility.

The PL spectrum of SWCNT sample was successfully obtained Fig.30. The measurement parameters were: 786nm and 13mW excitation, 1.6 kHz scanner velocity, 20 cm^{-1} resolution and 1 minute measurement time. For such parameters SNR$_{FT}$ = 3000 is obtained.

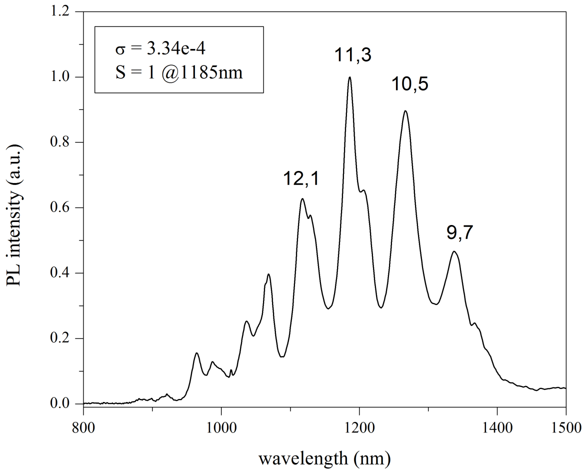

Figure 30: PL spectra of SWCNT sample at 786nm excitation as measured with the FT-PL spectrometer. The chirality peaks are denoted.

3.2.2 The Flicker noise

I find that the dominant noise contribution is the flicker noise of the signal. This has a profound impact on the utility of the FT technique, as the flicker noise is not distributed evenly in the FT-spectrum, contrary to the detector- and shot noise.
The flicker noise is caused by the power instability of excitation. It can be easily identified by measuring the noise as function of the frequency at given power at the sample, or as function of the power at the sample as function of frequency. A $1/f$ characteristic is expected for the sooner, and a linear characteristic is expected for the later. I measured the power dependence of the noise on the Ge detector output with a Lockin amplifier.

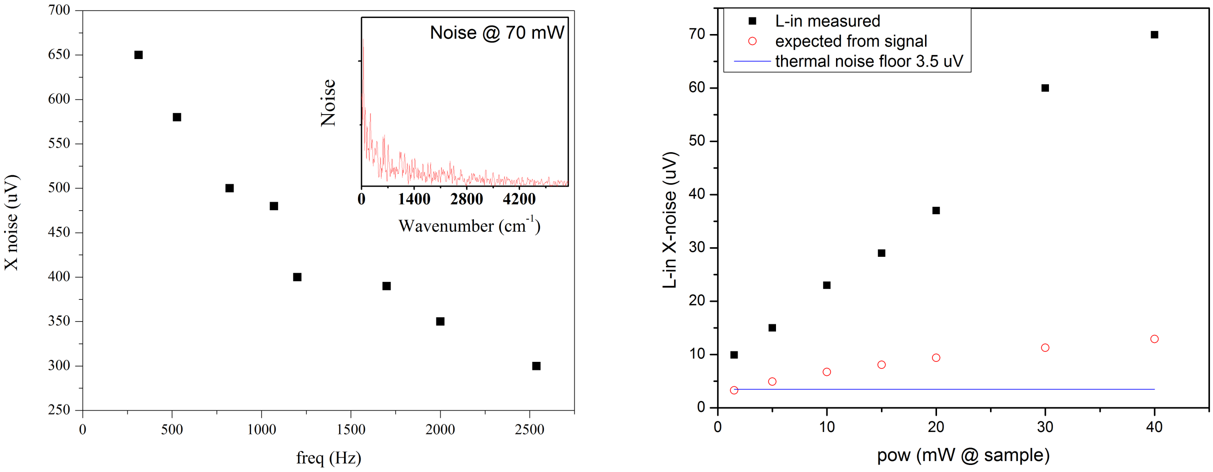

(a) Fig. 1

(b) Fig. 2

Figure 31: Noise measurement of SWCNT PL spectra of our FT-PL setup. a): frequency dependence of the noise at 70mW sample irradiation. The amplitude monotonically decreases, which is typical for flicker noise. The inset shows the low wavenumber region of the PL spectrum where no PL lines are observed. The noise shows $1/f$ dependence. b): irradiation power dependence of the noise shows linear relation (black squares) again typical for flicker noise. The shot noise contribution is calculated from the measured signal (red circles). The thermal noise floor is denoted by a red line. The noise is dominated by the flicker noise at every power.

In Fig.31(a) I show the frequency dependence of the noise at 70mW sample irradiation (786nm). It is clear, that the noise monotonically decreases, however, the characteristic is not clear. In the inset I show the first part of the PL spectra near the DC. There, we do not observe PL lines, however the $1/f$ noise is clearly seen. It corresponds to the signal of $k = 0cm^{-1}$, which corresponds to $0Hz$, i.e. it is the noise of the baseline of the interferogram. In Fig.31(b), I show the noise of the Ge detector at various laser powers measured at 1kHz. The linear dependence of the noise is clear. The calculated shot noise data (red circles), and the constant detector line (blue line) is also illustrated. Shot noise was calculated from the measured interferogram baseline (the Ge detector gain and responsivity is known from the datasheet). The measured data indicates that the flicker noise dominates our measurement at nearly every possible laser power. We also find from the calculated shot noise, that the PL measurement would be shot noise limited if we somehow suppress the flicker noise. This means that even with zero flicker noise, the Fellgett advantage is degraded (same case as shot noise limited broad band spectra, in case of VIS-FT), despite the fact that the spectrum is located in the NIR regime, which is usually ideal for the FT instrumentation. This is expected as the PL is a strong process contrary to the Raman scattering.

The flicker noise limited measurements are well known in the field of electronic detectors and oscillators. However, this limit can be tackled by using heterodyne mixing technique e.g. Lockin detection. There the signal to be detected is mixed up to a high frequency carrier, where the flicker noise has already decayed (due to the $1/f$ characteristic). However, the case in our setup is not similar, as here the signal itself is flicker noise limited (via the unstable source) and not the detector. This means that mixing up the signal (e.g. using an optical chopper or modulator) is useless as therein the low frequency noise components are also mixed up to near the carrier along with the signal, i.e. the flicker noise appears as a sideband adjacent to the modulation frequency.

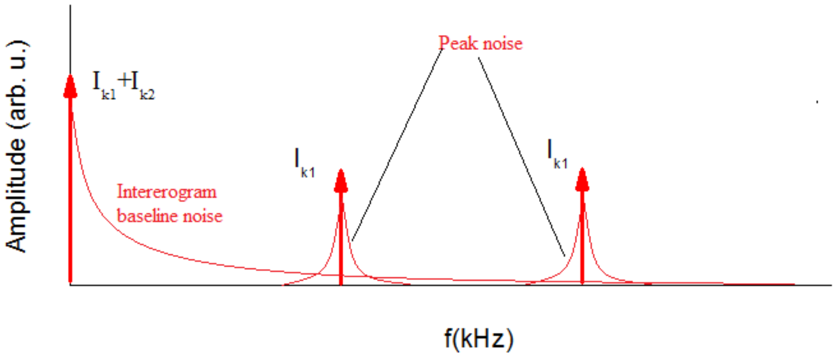

Figure 32: Schematics of the evolution of the flicker noise in the FT technique. A large flicker noise contribution appears at low frequencies (1/f) due to the baseline of the interferogram. The flicker noise coming from the individual peaks appears as sidebands to the spectral lines.

This effect was theoretically studied by Vogtman *et. al.* [36], and experimentally by G. Horlick *et. al.* [37].

The transformation of the flicker noise along with the signal in the spectrum has a non intuitive effect: the SNR is constant across the spectrum Fig.33. The amplitude of the flicker noise is linear in the power Fig.31(b), thus strong peaks have large flicker noise and weak peaks have weak noise, i.e. the SNR is the same for any spectral line.

Similar behavior was observed for our FT-PL spectrometer Fig.34. A large $1/f$ noise is observed at low wavenumbers, that I assign to the flicker noise contribution of the interferogram baseline. The flicker noise contribution of the PL lines is clearly present. Finally, I note that the SNR of the spectrum is constant along the spectrum and it assumes the value SNR ≈ 50. This is to be compared with SNR $= 3000$ (Fig.30), where the noise is taken from the baseline. We see indeed, the flicker noise severely limits the SNR.

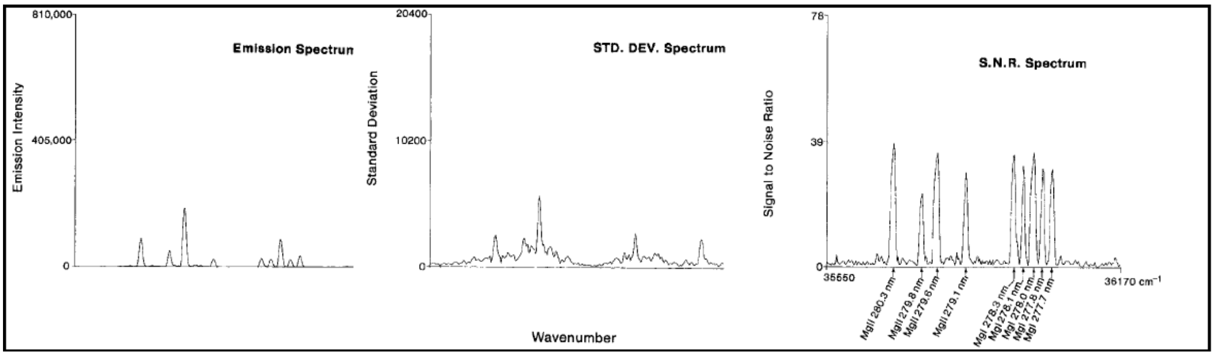

Figure 33: Flicker noise limited optical spectrum, detected with FT-spectrometer from Ref.[37]. The signal, the noise and the SNR are separately depicted. STD. DEV. spectrum: noise resides on the spectral peaks. The SNR is independent of the peak amplitude, and is constant across the spectrum.

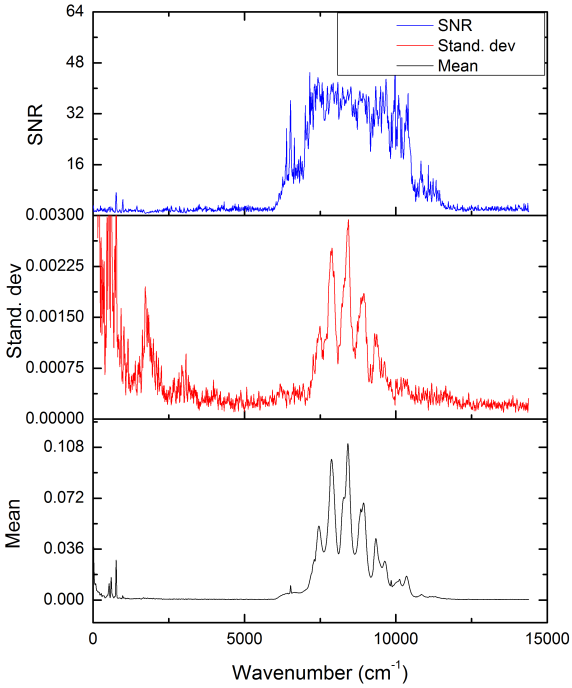

Figure 34: The evolution of the signal, noise and SNR of SWCNT PL spectrum measured with FT-PL spectrometer done at (788nm 12mW, SWCNT sample 1x6kHz $20cm^{-1}$ resolution. The statistics were made based on 12 scans. The spectrum in the middle shows that the noise is larger on top of the spectral lines.

The flicker noise is given as Relative Intensity Noise $RIN = 10log(\frac{P_{\text{noise}}}{P_{\text{carrier}}})$ and given in the units of dBc, where $P_{carrier}$ is the output power of the laser at some carrier frequency (0 Hz in our case). I managed to reduce the flicker noise of the laser by the following steps:

1. The Ti:Sapp laser should be used at 5 or 6 W pumping power. The power at the sample should be externally attenuated. When used with lower puping power, the flicker noise increases.

2. External attenuation should be done by inserting a pinhole. Absorbers are not a good choise since the output intensity of the laser is typically 600-700 mW.

3. External attenuation could be also achieved by using an interference filter. However, this makes the laser intensity even noisier, as there, the frequency instability of the laser is converted to amplitude instability, due to the ultra steep filtering edge.

4. The RIN depends on the number of the Lyot filter Quartz plates. Increasing the plate number decreases the noise (see Fig.35(a)).

5. Every mechanical part must be well fixed, especially the external attenuation pinhole (see Fig.35(b)).

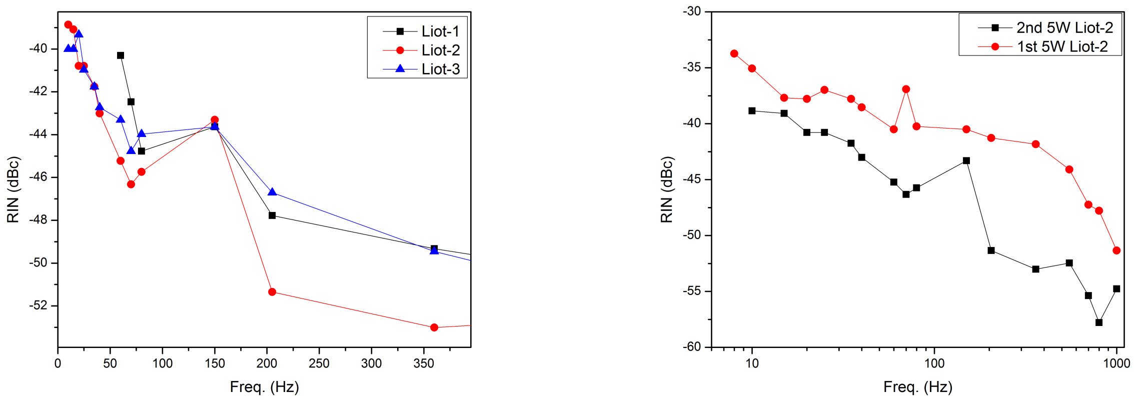

(a) Fig. 1

(b) Fig. 2

Figure 35: Fig. 1. shows the RIN for the Lyot filter used with 1, 2 and 3 Quartz plates. For low frequencies, where the flicker noise is dominant, the 2 and 3 plates filter is better than the single plate. I found an intensity instability at 150 Hz for all three filters, this I attribute to the laser resonator. Finally for high frequencies, a Liot filter with two Quartz plates seems to work better, however, there the flicker noise decays and the shot noise is dominant. Fig. 2: When every mechanical part of the optics is fixed (black), the flicker noise is somewhat reduced.

The flicker noise of the laser can be significantly reduced by applying a so-called Noise Eater. It is an active instrument that stabilize the laser power by dynamically attenuating it, where the time dependent attenuation is controlled by a feed-back error signal. The error signal is constructed by coupling out a small portion of the incoming laser beam and comparing it with a predefined value Fig.36. The transmission of a liquid crytal medium is then modulated with this feedback signal so the output power is held as stable as possible. In Fig.36, I show the the frequency dependent attenuation curve of a *Thorlabs LCC3112H* Noise Eater, that I used to reduce the flicker noise. For low frequency regime, where the flicker noise is dominant, the noise can be attenuated by a factor of 100x.

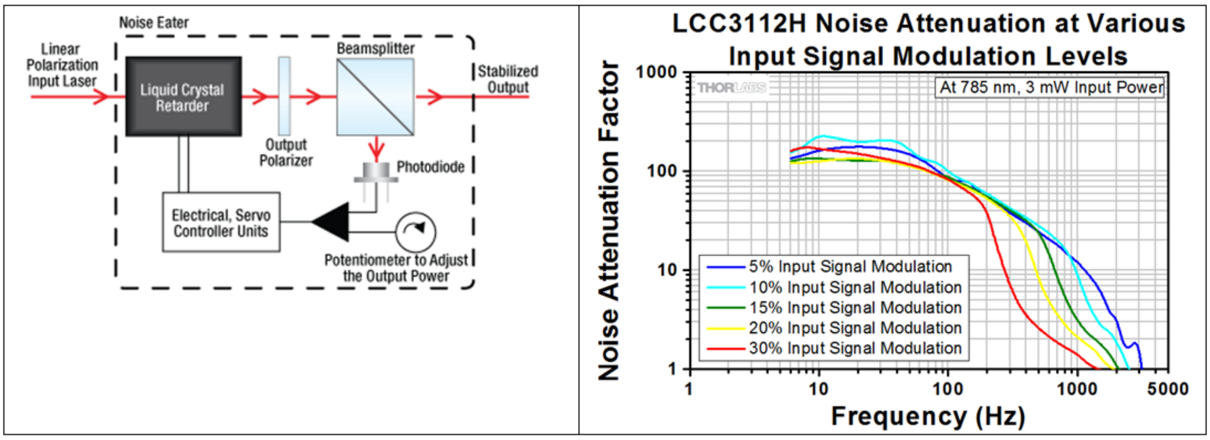

Figure 36: Left: The schematic build-up of the noise eater. The intensity is stabilized by feeding back an error signal to a liquid crystal attenuator. Right: frequency dependent attenuation of the applied Noise Eater.

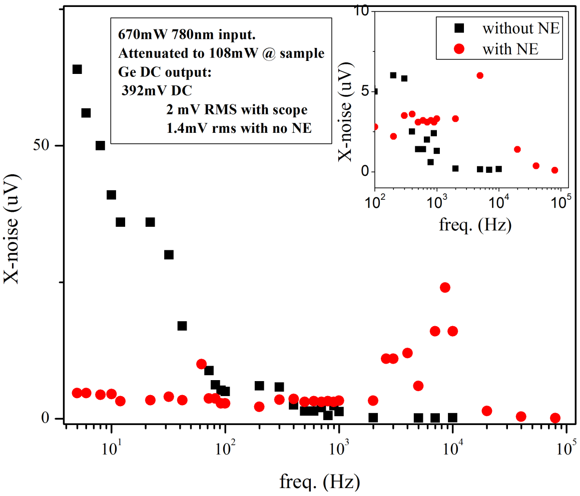

Figure 37: Output power noise of the Ti:Sapp laser measured as function of the frequency with and without utilizing the NoiseEater

In Fig.37, I show the measured Ti:Sap output power noise with and without noise eater. For low frequencies (up to 100Hz) the noise attenuation is excellent. However, I learned that for frequencies above 600 Hz the noise attenuation factor not only decreases

Fig.36, but becomes even noisier than without applying it Fig.37 inset. This is due to the instability of the error feedback in the Noise Eater itself for high frequencies. This results in a 30% increase in the total rms noise, when the full 3.3 kHz measurement BW of the Ge detector is considered (see Fig.37 inset). In conclusion: applying a Noise Eater does not pay off as although the low frequency noise decreases, the high frequency part grows. Assuming a broadband measurement, the total noise is increased, thus the Noise Eater would be helpful for only the dispersive measurement as there, the BW is 10 Hz.

3.2.3 Comparison to dispersive PL-spectrometer

The performance of the FT-PL spectrometer was compared to a dispersive single channel *Jobin Yvon iHR 320* equipped with 600 groove/mm diffraction grating and an InGaAs detector (*IGA1.9*) that I characterized (See AppendixA).

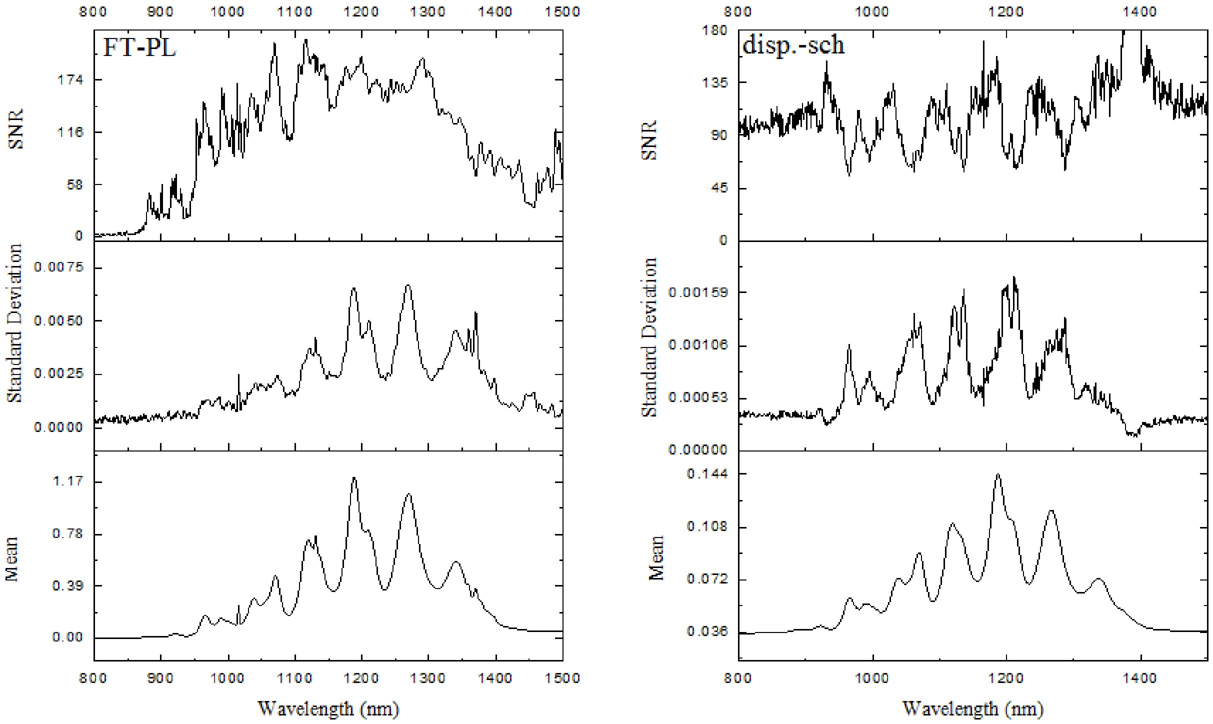

Figure 38: PL spectrum of SWCNT sample along with the noise spectrum and the SNR spectrum for FT-PL (left) and dispersive single channel (right). The noise spectrum seggests a flicker noise limit for both methods. The FT-PL SNR is somewhat better, but generally no significant difference is observed. Statistics was based on 12 measurements for each spectrometer.

The comparison is presented in Fig.38. Twelve spectra (each measured for one minute) were averaged to determine the standard deviation. The measurements were done at 786nm 12mW and 1.6 kHz mirror velocity in case of the FT-PL spectrometer. The input slit was set to the maximum value in case of the disp.-sch, and the resolution was set to 20 cm^{-1} in case of FT-PL, as the linewidth is limited by the physical process and not the instrument. We see that the flicker noise also effects the disp.-sch spectrometer, as seen from the wavelength dependent noise. The SNR of the two techniques are roughly equal. I conclude that no significant improvement in the sensitivity can be achieved with the FT-PL.under the given circumstances, i.e. a flicker noise dominated laser source.

Finally, the fact that the FT-PL measurements are flicker noise limited does not automatically mean the same limit for an FT-ODMR spectrum. We see in Fig.32 that the flicker noise is transformed (in the spectrum) to where the signal is. However, the noise amplitude is linear with spectral line intensity, i.e. for FT-ODMR where the spectral lines are very weak the dominant noise will be the broad band shot-noise, thus we expect a Fellgett advantage.

3.3 Improving the dispersive PL spectrometer

I showed in the previous section that the PL measurements for our dispersive and FT setup are flicker noise limited. However, the flicker noise is only dominant at high laser power levels, which is demonstrated in Fig.20. At low power levels either the detector noise or the shot noise is the dominant noise source, thus applying a sensitive photo detector would increase the SNR of the measurement. I characterized the available NIR photodetectors in our lab (see Appendix A), to find which one of them is the most suitable for PL measurements at low laser powers. I found that the large area Ge photo-diode used for the FT-IR setup has superior parameters (sensitivity, noise and BW) compared to that applied in the dispersive spectrometer. In the following, I discuss how the sensitivity of the dispersive PL spectrometer can be enhanced with the use Ge photo-detector is. The dispersive Jobin-Yvon spectrometer was supplied with a photodetector having a low power sensitivity of $10^{-14}\mathrm{W}/\sqrt{\mathrm{Hz}}$, whereas the Ge detector has a sensitivity of $10^{-15}\mathrm{W}/\sqrt{\mathrm{Hz}}$

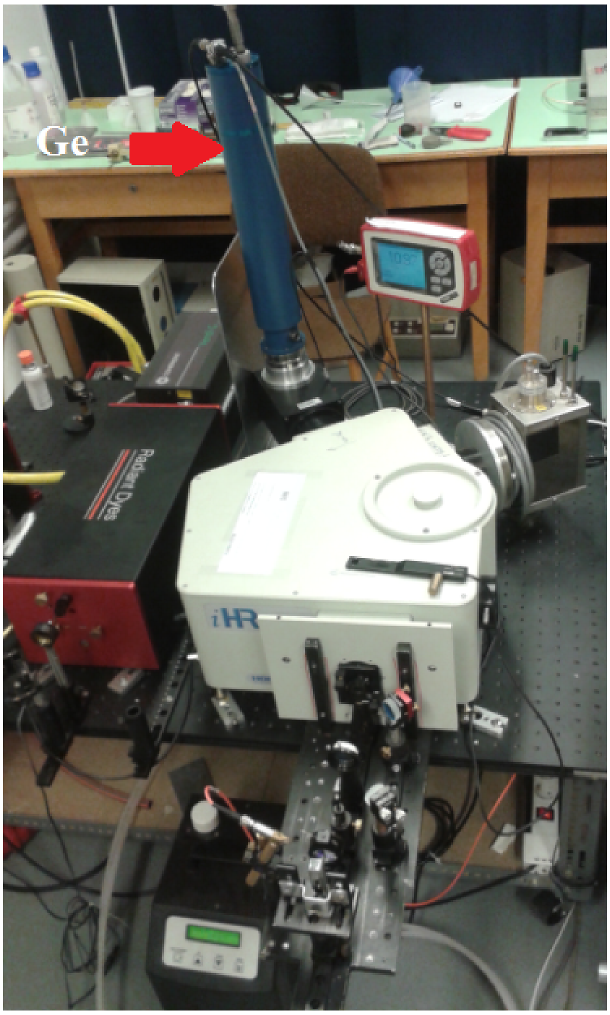

Figure 39: A photo of the *Jobin Yvon iHR 320* with the utilized Ge detector.

In Fig.40, I show the PL spectrum of SWCNT sample measured with InGaAs and Ge detectors at high and low laser powers. At high powers, the quality of the detector is

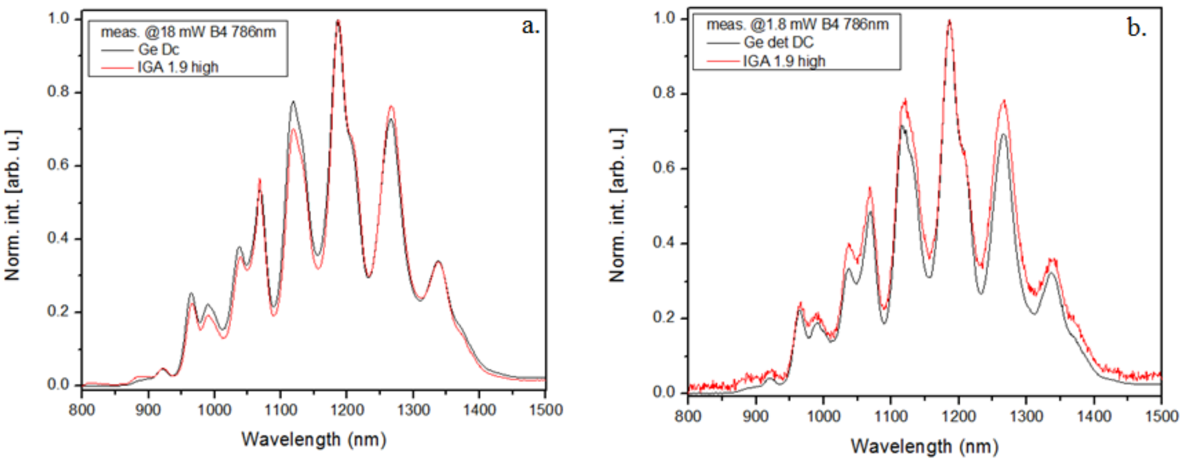

Figure 40: PL spectrum of SWCNT sample measured at high (a.) and low (b.) laser powers. Measurements were done with the dispersive spectrometer using two detectors: The supplied InGaAs and Ge photo-detector. The SNR measured with Ge detector is better at low laser power.

irrelevant, as there the flicker noise sets the limit Fig. 40a. However, for low laser power, the SNR performance of the Ge detector is clearly superior.

The nature of the noise is also investigated. Measuring the power dependent noise Fig.41(a) indicates flicker noise at low frequencies and shot noise at high frequencies. The frequency dependent noise was also measured at two laser powers Fig.41(a). The shot noise limit sets in much sooner for low laser powers

In conclusion, applying the more sensitive Ge photo-detector instead of the InGaAs photodiode supplied by the manufacturer improves the SNR performance of the dispersive spectrometer. The improvement is significant at low laser powers.

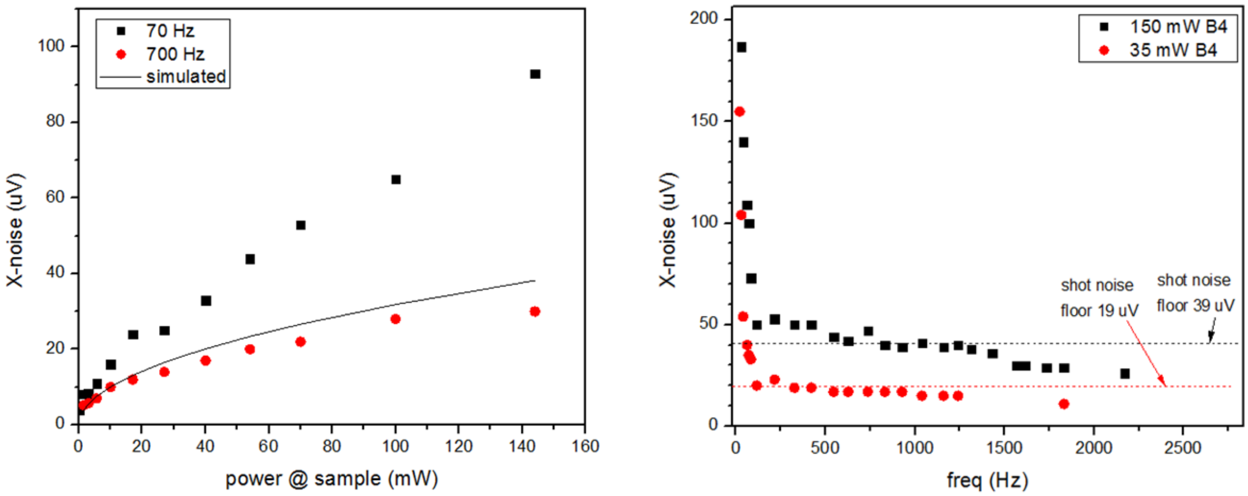

(a) Fig. 1

(b) Fig. 2

Figure 41: Fig. 1. Power dependent noise of the Ge detector at two frequencies. For low frequency the trend is linear indicating flicker noise. A square root dependence is observed at 700 Hz indicating strong shot noise contribution. Calculated shot noise (from the detected signal amplitude) agrees well with the measured noise (continuous black line). Fig. 2: Frequency dependent noise of the Ge detector at two laser powers along with the calculated shot noise (dashed lines). The shot noise limit sets in sooner at low power. Noise decrease above 1.5 kHz is due to the cut-off of the detector (-6dB@3kHz)
.

4 Summary

In this thesis I present the development of an FT-Raman spectrometer working with a visible laser excitation. I show, that the nature of the Fellgett advantage depends heavily on the character of the spectrum. For Raman like spectra, where few, well defined narrow peaks compose the spectrum the Fellgett advantage is conserved even in the shot noise limit case. I critically compare the performance of the FT-PL spectrometer to a home built single channel- and a state-of-the-art multichannel dispersive spectrometers. I found that the performance of the FT-PL spectrometer is superior to that of the single channel one and comparable to the CCD based method. Finally I discuss that the true advantage of the FT-PL spectrometer is the immense room to increase the exciting laser power, and with it the SNR of the spectrum. This part of the work was published in Ref.[10].

In the second part of the thesis I present the development of and FT-PL spectrometer working in the NIR regime. The setup serves as the first step to develop an FT-ODMR spectrometer. I show that the sensitivity of the spectrometer is limited by the flicker noise. I discuss the effect of the flicker noise on the SNR PL spectrum. Due to the multiplex effect, the noise is not dispersed evenly in the spectrum, but it is rather located on the peaks of the spectrum, resulting in a uniform SNR value. I show how can the flicker noise be reduced by e.g. better laser alignment or using Noise Eater. The performance of the FT-PL spectrometer is compared to the dispersive spectrometer. I found, that both have similar sensitivity. Finally, I show that the SNR performance of the dispersive spectrometer can be enhanced by applying a sensitive Ge detector, especially at low laser powers.

Appendix

A Low noise photo detectors

VIS detectors

I use a photomultiplier tube in the development of the visible FT-Raman spectrometer. In order to understand the magnitude of the detected signal and the nature of the noise, the detection principle must be understood. A PMT detector is based on the phenomenon of photoemission of metals. The incident photon is absorbed in a layer capable of photo emission (usually Multialkali layer), this is called the photocathode. The cathode is followed by a series (typically 9 or 10) of Multialakali electrodes (dynodes), where voltage is applied between every dynode pair and at the end there is the anode. An emitted photo-electron is accelerated due to the voltage applied between the dynodes, when the electron hits a dynode, secondary electrons are emitted and further accelerated towards the next dynode, the process continues till the amplified current reaches the anode.

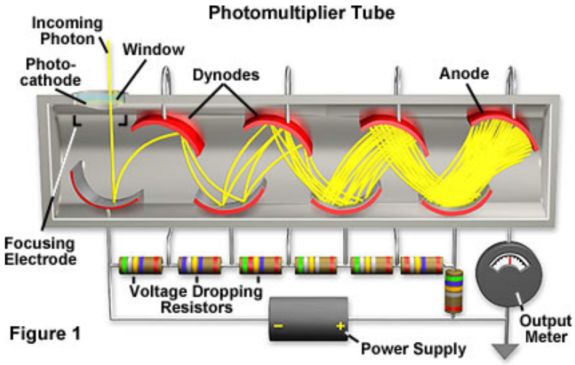

Figure 42: Schematics of the mechanism of a PMT. The emitted photo-electron is accelerated, emitting secondary electrons on the dynodes. At the end, a measurable current is present on the anode [40].

The ability of the photocathode to emit photoelectrons is given by the quantum efficiency (QE). QE is the propability of a photon to induce a photoelectron and usually varies between $10-20\%$, depending on the wavelength of the radiation Fig.42. The overall sensitivity of the cathode is described by the cathode radiant sensitivity in mA/W units, which gives the generated cathode current due to the incident radiation power Fig.43.

The voltage applied between the dynodes can be adjusted linearly with applying control voltage. Depending on the ability of the of secondary electron emission of the dynodes and the applied voltage, the sensitivity of a PMT is given by the gain factor g which shows that with given cathode current I_c -induced by the absorbed photons-, the anode current will be $I_a = g \cdot I_\text{c}$ Fig.43. The work function of a typical metal is about 2 eV. A visible photon has sufficient energy to generate a photoelectron. Then the electron is accelerated typically to 100 eV until it reaches the next dynode, and it thus generates about 5-10 secondary electrons. This gives rise to a typical gain of up to $10^7 - 10^8$. Photomultipliers are characterized by a dark current which is the result of some thermally excited electrons which leave the cathode. The dark current scales exponentially with the current, i.e. cooling of PMTs down to -30 C° is customary. The fluctuation of the dark current can be regarded as detector noise, however its magnitude is much smaller than that of NIR detectors, due to the much larger work function of the cathode. In a typical experiment the dominant source of noise for a PMT is shot noise. It is important to note that the shot noise is given by the cathode current, i.e. by the statistical fluctuation of the emitted primary electrons. It can be shown that the additional dynodes do not give a substantial contribution to the PMT shot noise.

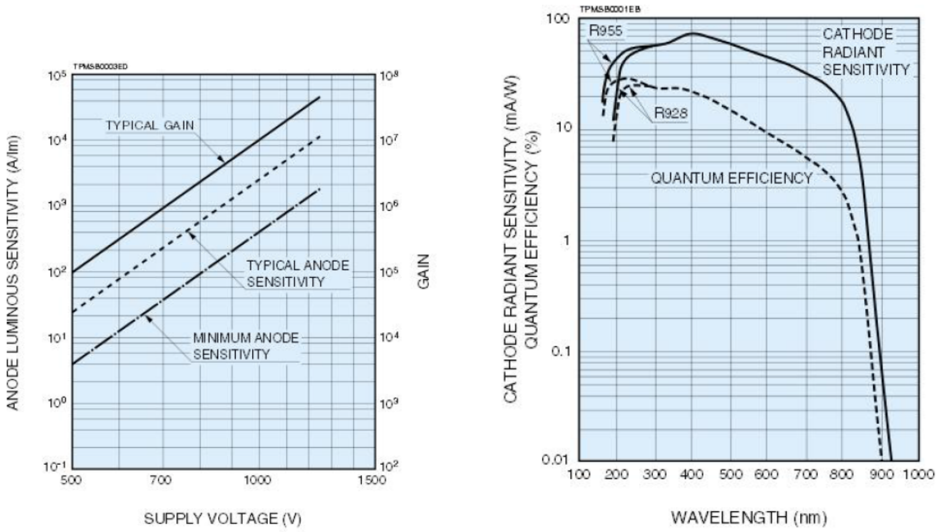

Figure 43: Left:The gain of the Hamamatsu R955 PMT as function of the applied voltage (dashed curve). Right: The QE and cathode radiant sensitivity of Hamamatsu R955 PMT as function of radiation wavelength[40].

NIR detectors

In my work I primarily dealt with spectra in the infra red (IR) regime. In this optical band several photodetectors exist such as: Charge Coupled Device (CCD), Photo Multiplier Tube (PMT) and Photo Diodes (PD). Which one of them is the best, is decided by the given application. The CCD is a truly multichannel detector, with high Quantum Efficiency, however it is limited by the read-out time, thus it is not suitable for fast measurements. PMTs are fast detectors ($BW \approx MHz$), however, they suffer from low Quantum Efficiency. The general buildup of a photodetecor is presented in Fig.45. The critical part of every low noise photodetector is the so-called *transimedence amplifier*, that serves as the preamplifier and I/V converter. It consists of an operational amplifier and a feedback loop that contains the feedback- resistor R_F and capacitance C_f. R_F determines all of the important parameters like BW, gain and the NEP of the photodetector.

The optical measurements in our lab: Raman, PL and ODMR - especially the later - require a fast, low noise and sensitive detectors. The corresponding parameters are the BW ([kHz]), Noise Equivalent Power ($W/\sqrt{Hz}$) and the Responsivity (V/W). To choose the best photo detector for PL and ODMR measurement, I characterized the three optical detectors that we have in our Lab Table.5. The measured characteristics are presented in

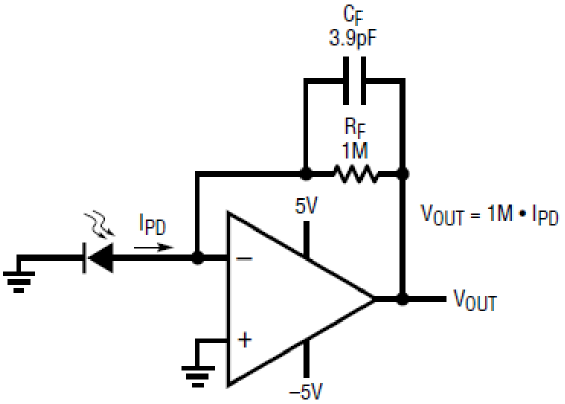

Figure 44: A typical construction of a photodetector. The photocurrent I_{PD} is amplified by the transimpedance amplifier. Figure from Ref.[41]

Horiba Jobin Yvon DSS-IGA1.9010L	InGaAs photo diode
Horiba Jobin Yvon DSS-IGA020L	InGaAs photo diode
Applied Detectors 403L	Ge photo diode

Table 5

Tab.6.

The parameters of the Ge detector stands out among that of the InGaAs detectors. This is due to the so-called *bootstrapping* circuit. Large area PDs come with large capacitance, that has a profound effect on the noise bandwidth of the device. By applying a low noise JFET before the transimpedance amplifier, the capacitance voltage of the diode is "bootstrapped", while I_{PD} passes to the transimpedance amplifier. Such solution is realized in the case of the Ge PD, and that is why a low NEP can be achieved while maintaining high BW and sensitivity.

I also changed the feedback resistance (with the help of Dr. Ferenc Fülöp) R_F of the IGA020 detector to better understand its impact on the BW, NEP, and gain and also to see whether these quantities could be changed to better fit our goals (measuring low inensity fast signals of the ODMR). The IGA020 detector comes with a $R_F = 1G\Omega$, this was subsequently changed to $100M\Omega$ and $10M\Omega$. I used two types of $100M\Omega$ resistor to see, whether the detector's characteristics depend on the R_F quality when having the same nominal reisitance value. These changes where tested on SWCNT PL spectra using 726nm laser, 150 mW, 10Hz BW Fig.46. We see, that the gain goes linearly with the value

detector	BW(-6dB point)	NEP $(W/\sqrt{Hz})$	Responsivity (V/W)
Ge	3 kHz	10^{-15}	$3.5 \cdot 10^9$
IGA 020	300 Hz	$2 \cdot 10^{-15}$	$2.5 \cdot 10^{10}$
IGA 1.9	2.2 kHz	$3 \cdot 10^{-14}$	$2 \cdot 10^9$

Table 6

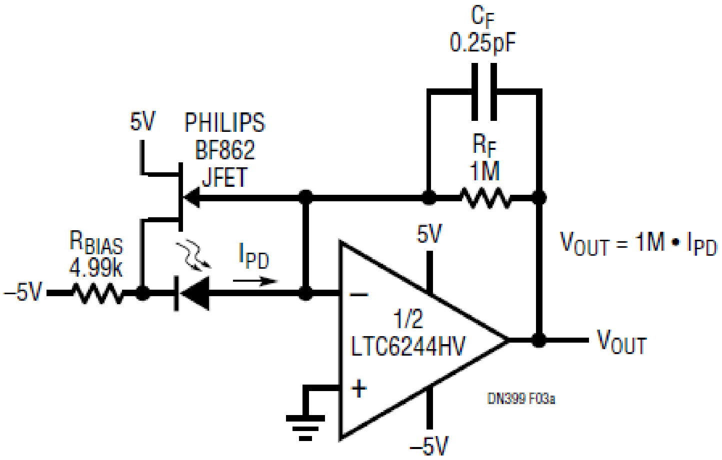

Figure 45: Before amplifying the photo current of the diode (transimpedance amplifier), I_{PD} is processed by a bootstrapping circuit: the low noise JFET bootstraps the capacitance voltage of the diode, so the output noise is reduced. Figure from Ref.[41].

of R_F. The noise level U_{RMS} did not change from $1G\Omega$ to $100M\Omega$, however, it drops with $\sqrt{R_F}$ from $100M\Omega$ to $10M\Omega$.

The BW of IGA1.9, IGA20 $1G\Omega$, IGA20 $100M\Omega$ and IGA20 $10M\Omega$ were measured. First IGA1.9 and the unmodified IGA20 ($1G\Omega$) are compared in Fig.47.

The original IGA20 ($1G\Omega$) was modified first by inserting $R_F = 100M\Omega$. We observe a factor of 5x increase in the BW, however, we did not anticipate any change in the noise level, that remained $15\mu V/\sqrt{Hz}$.

By changing R_F from 100 to 10 $M\Omega$, we observed a factor of 3x increase in the BW Fig.49, but also the noise level dropped from $14\mu V/\sqrt{Hz}$ to $5\mu V/\sqrt{Hz}$ i.e. it scales with $\sqrt{R_F}$.

Going from $100M\Omega$ to $10M\Omega$ in case of IGA20 suggested that the impact of R_F on the BW and NEP goes as Eq.(25).

$$\begin{aligned} NEP &\propto \sqrt{R_F} \\ BW &\propto \frac{1}{\sqrt{R_F}} \\ NEP \cdot BW &= const \end{aligned} \tag{25}$$

However, this was not true when going from $1G\Omega$ to $100M\Omega$. This suggest that not only the nominal value of R_F determines these quantities, but also the "quality" of the resistor. To test this we changed the resistor in IGA20 from $100M\Omega$ to another $100M\Omega$ one produced by another company (better quality) Fig.50.

To conclude this section: I characterized the three optical detectors that were available in our lab, in order to choose the most suitable one for low intensity fast optical detection. The three most important quantities are NEP, BW and sensitivity. All of them can be altered by replacing the feedback resistance of the transimpedance amplifier, however these three parameters remains interconnected, and the trade-off between them are described

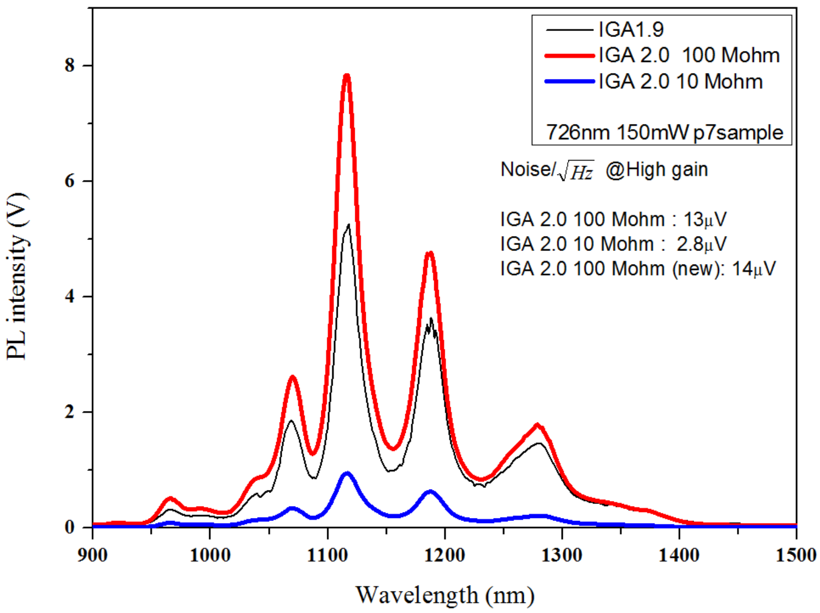

Figure 46: SWCNT PL spectra with detector IGA020 at different T_F values.Red curve corresponds to $100M\Omega$. By applying $10M\Omega$, the gain also drops by a factor of 10x (blue line). We also observe a drop in the NEP, measured at frequencies below the cut-off frequency. Measurement with IGA1.9 were done for reference.

by Eq.(25). Also the quality of the R_F has a profound impact on the BW and NEP. Finally, The bootstrapping solution of the Ge detector makes is the most fitting detector for our purposes, as it can maintain high BW and Gain while achieving low NEP.

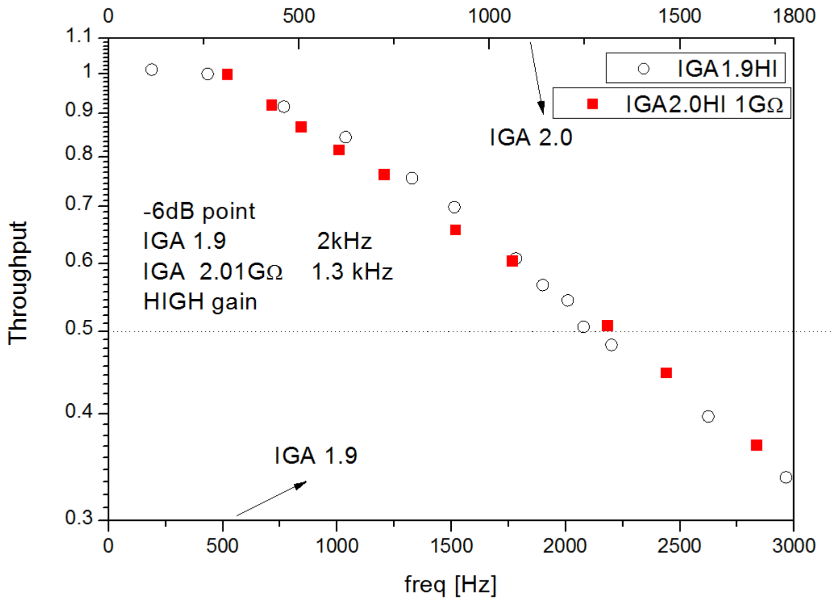

Figure 47: Measured BW for IGA1.9 and IGA20 1$G\Omega$. IGA1.9 has BW=2kHz 1.5x greater than IGA20 1$G\Omega$. However, it has an inferior NEP and sensitivity Tab.6

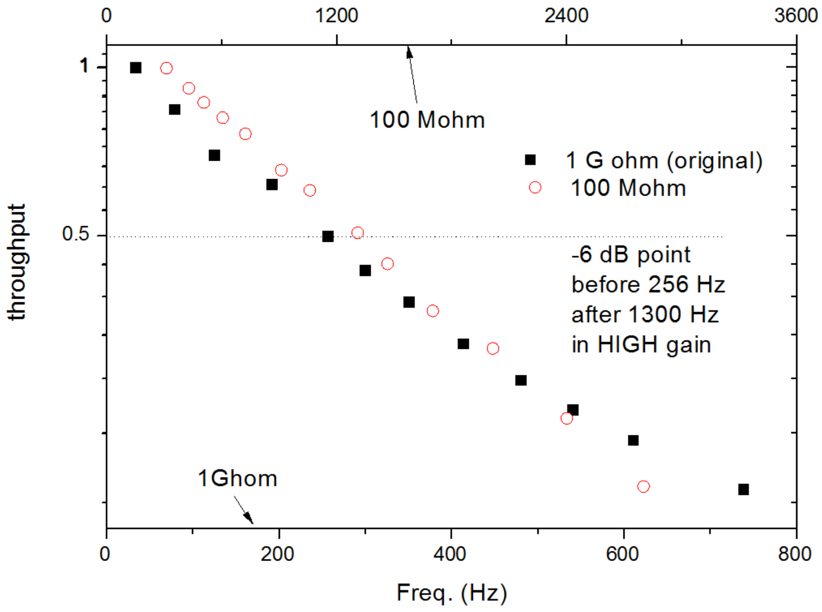

Figure 48: Measured BW of IGA20 1$G\Omega$ and IGA20 100$M\Omega$. We observe a factor of 5x increase in the BW. However the noise level remained unaffected Fig.46.

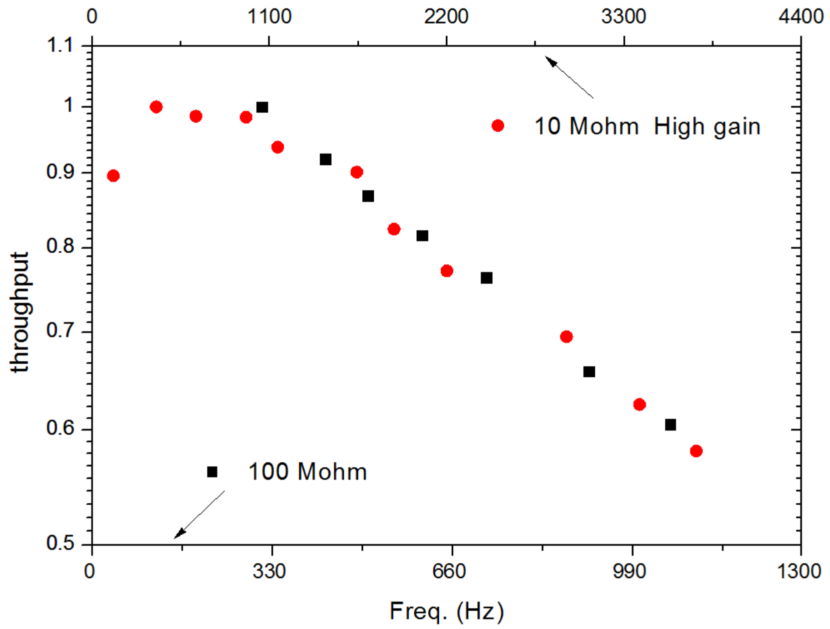

Figure 49: Measured BW of IGA20 $100M\Omega$ and IGA20 $10M\Omega$. We observe a factor of 3x increase in the BW. The noise level also scales with $\sqrt{R_F}$ see Fig.46.

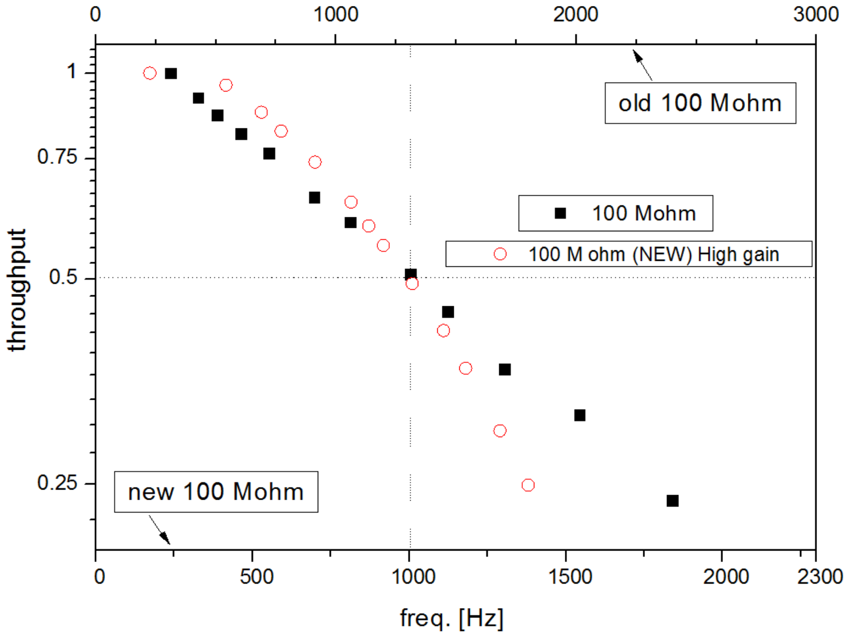

Figure 50: Measured BW of IGA20 $100M\Omega$ for two different resistors with the same nominal value but different qualities. The noise level did not change. The measured voltage noise density did not change ($14.8\mu V$.) However, the cut-off frequency did change by 20%, also the characteristic curve of the cut-off curve became much steeper, which would imply that the overall noise is changed, thus it has an effective noise BW.

B Principle of FT-ODMR

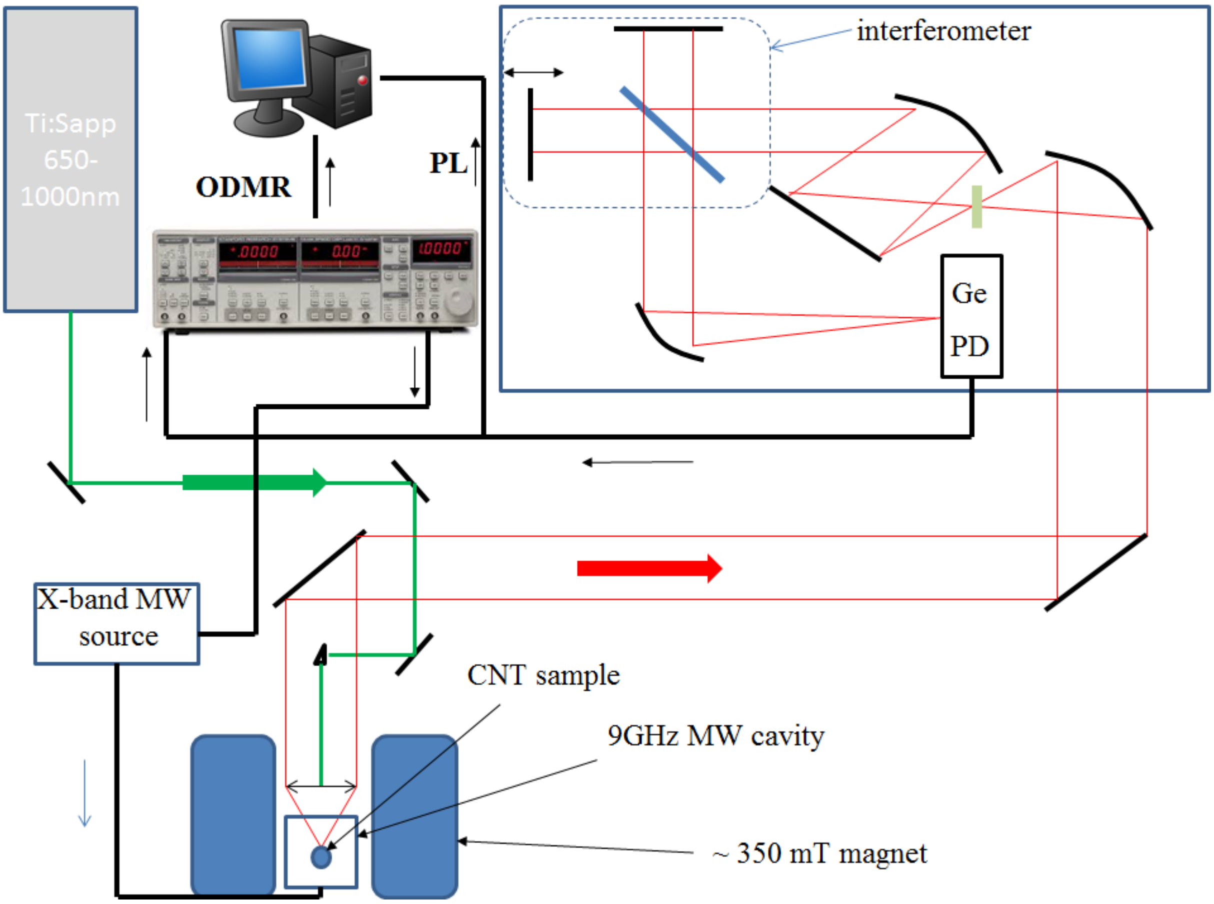

Figure 51: Schematics of the FT-IR spectrometer used to collect PL and ODMR spectra of SWCNTs. The setup consist of three main parts. The excitation/collection part includes mirrors and lenses to realize the optical path of the excitation (green) and scattered light collection (red). The microwave (MW) setup includes the sample and realizes the ODMR process. Finally the optical path is coupled to an FT-IR spectrometer (*Bruker IFS 66v*) including a Michelson interferometer and Ge photodetector. The detector signal can be directly processed to acquire the PL spectrum (PL branch) but it is also processed by a Lockin amplifier to record the ODMR spectrum

The schematics of the FT-PL and FT-ODMR spectrometers are presented in Fig.51. The first unit out of three is the laser excitation- and light collection optical path. The setup is suitable to simultaneously measure PL and ODMR spectra as the spectrometer output can be directly connected to the PC to measure PL, or it can be further processed by a Lockin amplifier to acquire the ODMR spectrum.

Although this work could not be completed within this thesis, I present the planned development of an FT based ODMR spectrometer. The FT-PL measurement can be thought of as a common Amplitude-modulation technique known from the viewpoint of signal processing. The intensity of the scattered light is constant in time, thus it's spectrum is a Dirac-delta centered at 0 Hz, whose amplitude is the integrated spectrum see Fig.52. The role of the interferometer is that it amplitude modulates each spectral component with an energy selective amplitude (spectral intensity $E(k)$) and modulation frequency $v_{mirror}k$ according ot Eq.(5). By setting the scanner velocity to 1.6 kHz, it assigns the 1.6 kHz modulation frequency to the 633 nm He-Ne (16000 cm^{-1} radiation) thus an SWCNT PL IR spectrum ranging between 10000-12000 cm^{-1} is modulated, so the electronic signal of the detector ranges between 1-1.2 kHz Fig.52, spreading the DC input to a broadband output Fig.52.

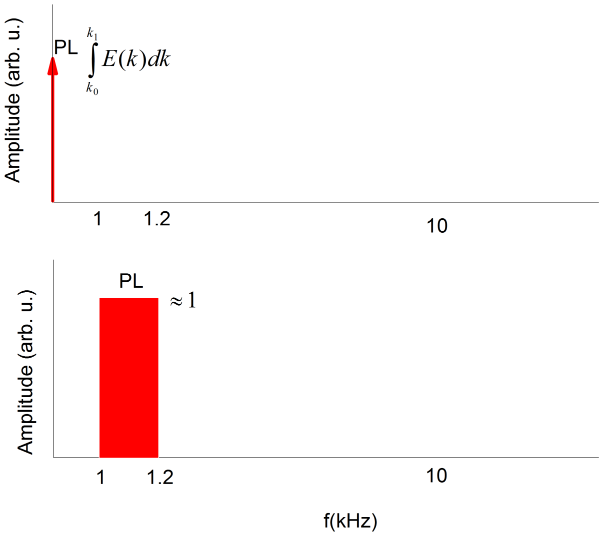

Figure 52: The intensity of the light at the entrance is a DC component with the integrated spectrum $E(k)$, where the spectrum is assumed to be a boxcar function (between k_0 and k_1) for simplicity. The interferometer amplitude-modulates the input in an energy selective manner, assigning a unique modulation- amplitude and frequency to light with specific wavenumber (lower fig.)

The ODMR process is induced by the presence of a DC magnetic field and a resonant microwave field. However, this is a very week process, 10^{-3} part of the PL intensity, thus it is hopeless to detect it by simply subtracting two spectra- one with the MW field on and one with the MW field off- so the ODMR contribution is seen- as the signal will be buried in the noise. This problem can be bypassed by applying *Phase Sensitive Detection*: a Lockin amplifier. Here the the resonant MW field is chopped, so the ODMR contribution appears as a very week modulation of the PL lines. The PL+ODMR output of the optical-detector is processed by a Lock-in amplifier -whose frequency is locked to the chopping frequency- that suppresses the PL contribution and amplifies the ODMR component.

The PSD detected FT-ODMR is visualized in Fig.53. Suppose we modulate the MW field with $f_{mod} = 10$ kHz frequency, then at the entrance of the interferometer, the signal will be a high DC (PL lines) and a small component at 10kHz Fig.53. By switching the interferometer on, the PL lines are transformed to the 1-1.2 kHz band, the ODMR signal appears as two branch of sidebands (each spread to about 200 Hz) separated by 1-1.2 kHz

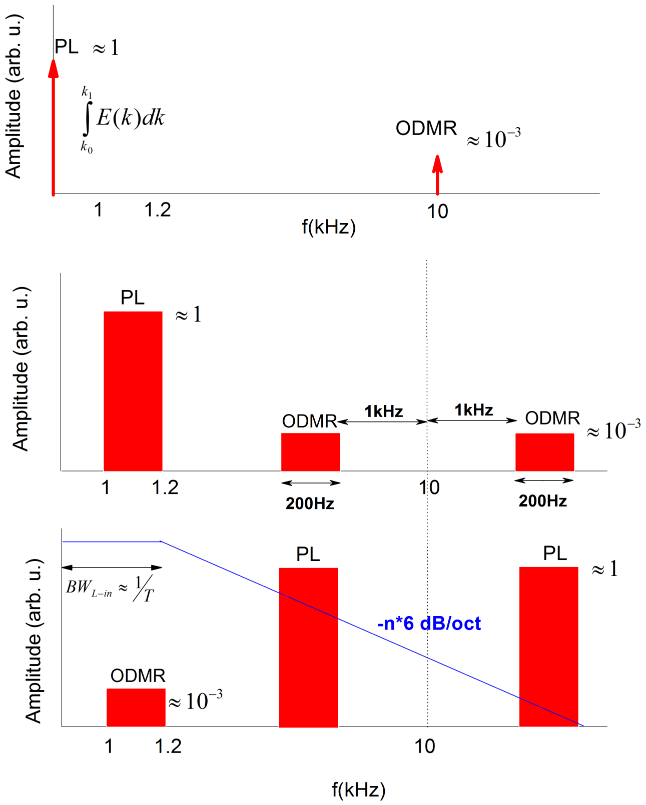

Figure 53: Upper figure:Similar to the case of FT-PL Fig.52, the intensity at the entrance of the spectrometer is a high DC of the PL. Due to the chopping of the MW field, the weak ODMR signal appears as a δ-delta at $f_{mod} = 10kHz$, but still spectraly unresolve. Middle figure: both the PL and the ODMR spectra are spectraly resolved at the output of the interferometer. The PL appears as a $200Hz$ wide boxcar function (for simplicity), 1kHz away from the DC. The resolved ODMR spectrum appears as a $200Hz$ wide satellites around f_{mod}, 1kHz away according to Eq.(26). Note the 10^{-3} factor in intensity, making the ODMR spectrum buried in noise. Lower figure: the spectrally resolved ODMR spectrum processed by a Lock-in amplifier.

around the 10 kHz chopping frequency Fig.53. To maintain simplicity. let us assume that the the ODMR spectra is only a 10^{-3} of the PL ($E_{ODMR}(k) = 10^{-3}E_{PL}(k)$), and let us select one specific (e.g. some kv_{mir}) line out of the $200Hz$ wide band where $E_{PL}(k) = 1$ and $E_{ODMR}(k) = 10^{-3}$. Then at the photodetector output the signal will be:

$$\begin{aligned} U(f) &= U_{PL}(f) + U_{ODMR}(f) = \cos(kv_{mir}t) + 10^{-3}\cos(kv_{mir}t)\cos(2\pi f_{mod}t) \\ U(f) &= \cos(kv_{mir}t) + \frac{10^{-3}}{2}\left[cos((2\pi f_{mod} - kv_{mirror})t) + cos((2\pi f_{mod} + kv_{mirror})t)\right] \end{aligned} \tag{26}$$

The lock-in amplifier multiplies $U_{ODMR}(f)$ in Eq.(26) with $cos(f_{mod}t)$, thus mixing the high frequency ODMR signal down to low frequency. The low frequency PL band is mixed up to high frequencies and appears as two side bands around f_{mod}. The Lock-in amplifier then filters out the high frequency band by applying a a Low Pass Filter (LPF)-whose filtering edge can bes set to $-n \cdot 6db/oct$ where $n = 1, 2, 3, 4$ so-called filtering order- and amplifies the week ODMR Fig.53.

Mathematically the Lockin amplifier output $U^*(f)$ is a multiplication of the input $U(f)$ with a modulation cosine and an filtering function $LPF(f)$. Also the output is amplified by a Gain factor G, depending on the sensitivity. The $LPF(f)$ function assumes the value 0 for very high frequencies like $4\pi f_{mod}$, some value between 0 and 1 for intermediate value $2\pi f_{mod}$, and ≈ 1 for low frequencies like kv_{mir}

$$U^*(f) = (U_{PL}(f) + U_{ODMR}(f)) \cos(f_{mod}t) \cdot G \cdot LPF(f)$$

$$\begin{aligned} U^*(f) = G \cdot LPF(f)\{cos[(2\pi f_{mod} - kv_{mir})t] + cos[(2\pi f_{mod} + kv_{mir})t]\} \\ +G10^{-3}\{cos(kv_{mir}t) + cos[(kv_{mir} + 4\pi f_{mof}t)] \end{aligned}$$

$$U^*(f) = G10^{-3} \cdot cos(kv_{mir}t) + G \cdot LPF(f)\{cos[(2\pi f_{mod} - kv_{mir})t] + cos[(2\pi f_{mod} + kv_{mir})t]\} \tag{27}$$

According to Eq.(27) the output spectra consists of the amplified ODMR spectra at low frequencies 1-1.2 kHz, and the filtered out PL satellites 1 kHz away from f_{mod}, see Fig.54.

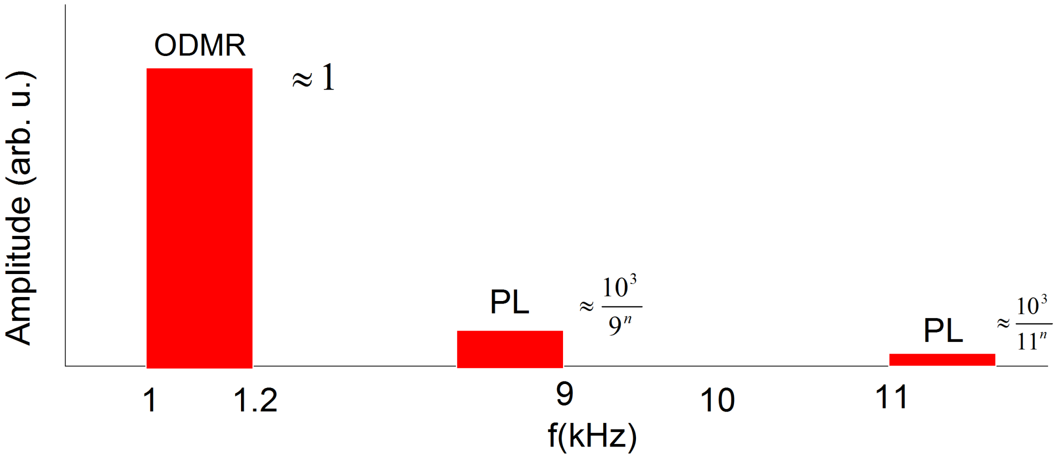

Figure 54: The spectrum of the Lockin amplifier output. The ODMR signal is mixed down from the high modulation frequencies close to DC between 1-1.2 kHz, and now is amplified. The PL lines are mixed up to higher frequencies forming a satellite arround f_{mod}. The PL amplitude is reduced by the filtering: assuming a BW = 1kHz the amplitude reduction is $\approx (\frac{BW}{f})^n$ where n is the filtering order.

Finally I note that contrary to most PSD detection techniques where a single frequency component is detected, here we want to measure a broadband spectrum, thus the Lockin output is not a DC signal Fig.54. The critical value here is the Lockin time constant.

The BW of the filter is $\propto 1/T$ where T is the Lockin time-constant, thus we have to choose it so the ODMR spectrum "fits in". This can be achieved by reducing the time constant, however this means an increase in the noise and a degradation of the ODMR spectrum (The Lockin can not average enough cycles). Increasing T will increase the SNR but will also reduce the BW i.e. it will average out the high frequency components of the spectrum. So we find that the lower value of the time constant should be between the ODMR line frequencies, which is determined by the mirror velocity (kv_{mir}) and the modulation frequency Eq.(28).

$$kv_{mir} < 1/T < f_{mod} \tag{28}$$

This can be only achieved by choosing a high f_{mod}, and a low optical modulation kv_{mir} i.e. low mirror velocities, so the Lockin time-constant can assume an intermediate value.

References

[1] E. Smith, G. Dent, *Modern Raman Spectroscopy: A Practical Approach*, Wiley, Chichester, 2005.

[2] D. B. Chase, *J. Am. Chem. Soc.*,**108**-7485. 1986

[3] T. Hirschfeld, B. Chase, *Appl. Spectrosc.*,**40**-133. 1986

[4] R. Savoie *et. al*, Mikrochim. Acta. **2**-223, 1988

[5] N. J. Everall *et. al*,Appl. Spectrosc. **43**-778, 1989

[6] C. J. Brenan *et. al*,Appl. Spectrosc. **49**-1086, 1995

[7] J. Zhao *et. al*,Appl. Spectrosc. **50**-1209, 1996

[8] J. Zhao *et. al*,Appl. Spectrosc. **50**-1687, 1997

[9] Hans Kuzmany, *Solid-State Spectroscopy*, Springer, 1998

[10] S. Dzsaber *et. al.*, J. Raman. Spectrosc., **46**:3, 2015

[11] Milán Negyedi, *Development of an Optically Detected Magnetic Resonance Spectrometer*, MSc. thesis, Budapest University of Technology and Economics, 2014

[12] R. S. Krishnan and R. K. Shankar, *Raman effect - history of the discovery*, J. Raman Spectr., *10*:1-8 1981

[13] M.S: Dresselhaus *et. al.*, *Raman spectroscopy of carbon nanotube*, Phys. Rep. **?**-?, 2004

[14] S. Hornbacker, *Electronic structure of carbon nanotube systems measured with scanning tunneling microscopy*, PhD dissertation, University if Illinois, 2003

[15] http://www.univie.ac.at/spectroscopy/fks/forschung/ergebnisse/nanotubes.htm

[16] M.D. Sturge, Phys. Rev. **127**-768, 1962

[17] Juan Yang *et. al.*, *Photoluminescence from Exciton Energy Transfer of Single- Walled Carbon Nanotube Bundles Dispersed in Ionic Liquids*, J. Phys. Chem **116**-22028, 2012

[18] http://micro.magnet.fsu.edu/optics/timeline/people/jablonski.html/

[19] J. C. Chacon-Torres , *Theory and Spectroscopy on functionalized Graphene and Graphite Intercalation Compounds*, PhD. thesis, University of Vienna, Vienna 2013

[20] B. Smith, *Fundamentals-of-Fourier-Transform-Spectroscopy 2nd edition*, Boca Raton: Taylor and Francis, 2011

[21] Vidi Saptari, *Fourier-Transform Spectroscopy Instrumentation Engineering*, Spie press, 2003

[22] S. Yu. Volkov *et. al.*, Sov. J. Quantum Electron. **11**-135, 1981

[23] Murphy Douglas B., *Fundamentals of light microscopy and electronic imaging pp. 66*, Wiley-Liss, 2001

[24] P. B. Fellgett, *RTheory of infra-red sensitivities and its application to investigations of stellar radiation in the near infra-red*, PhD Thesis, University of Cambridge , 1949

[25] T. Hirschfeld, *The Implications of Fluctuation Noise in Multiplex Spectroscopy*, Appl. Spectr. **30**:2, 1976

[26] S. Marra and G. Horlick, *Signal-to-Noise Ratio Characteristics of an Inductively Coupled Plasma/Fourier Transform Spectrometer*, Appl. Spectr. **40**:6, 1986

[27] J. Johnson, *Thermal Agitation of Electricity in Conductors*, Phys. Rev. **32**-97, 1928

[28] H. Nyquist, *Thermal Agitation of Electricity in Conductors*, Phys. Rev. **32**-110, 1928

[29] O. Llopis *et. al.*, *Photodiode 1/f noise and other types of less known baseband noises in optical telecommunications devices* doi 10.1109/ICNF.2013.6579014 Publisher: IEEE

[30] G. Fabian *et. al.*, , Rev. Sci. Instr. **82**-023905, 2011

[31] X. Baillard *et. al.*, Opt. Commun. **266**-609, 2006

[32] F. Robben, *Appl. Opt. 10*:4, 1971

[33] R. Savoie *et. al.*, , Mikrochim. Acta. **2**:223, 1988

[34] B. Lyot, *Optical apparatus with wide field using interference of polarized light*, Acad. Sci. **197**, 1933

[35] http://erewhon.superkuh.com/library/Space/Solar%20Polarimeter%20Design/

[36] E. Voigtman et. al., *Appl. Spectrosc.*,**41**-7. 1987

[37] G. Horlick et. al., *Appl. Spectrosc.*,**40**-6. 1986

[38] http://www.edmundoptics.com/technical-resources-center/imaging/limitations-on-resolution-and-contrast-the-airy-disk/

[39] http://www.horiba.com/scientific/products/optics-tutorial/monochromators-spectrographs/

[40] Michael W. Davidson Mortimer Abramowitz. Concepts in digital imaging technology: Photomultiplier tubes. http://learn.hamamatsu.com/articles/ photomultipliers.html, 2012.

[41] http://www.linear.com/solutions/1199